

# A simple embedded discrete fracture-matrix model for a coupled flow and transport problem in porous media

Lars H. Odsæter<sup>a,\*</sup>, Trond Kvamsdal<sup>a</sup>, Mats G. Larson<sup>b</sup>

<sup>a</sup>*Department of Mathematical Sciences, NTNU Norwegian University of Science and Technology,  
Alfred Getz' vei 1, 7491 Trondheim, Norway*

<sup>b</sup>*Department of Mathematics and Mathematical Statistics, Umeå University, SE-901 87 Umeå, Sweden*

---

## Abstract

Accurate simulation of fluid flow and transport in fractured porous media is a key challenge in subsurface reservoir engineering. Due to the high ratio between its length and width, fractures can be modeled as lower dimensional interfaces embedded in the porous rock. We apply a recently developed embedded finite element method (EFEM) for the Darcy problem. This method allows for general fracture geometry, and the fractures may cut the finite element mesh arbitrarily. We present here a velocity model for EFEM and couple the Darcy problem to a transport problem for a passive solute. The main novelties of this work is a locally conservative velocity approximation derived from the EFEM solution, and the development of a lowest order upwind finite volume method for the transport problem. This numerical model is compatible with EFEM in the sense that the same computational mesh may be applied, so that we retain the same flexibility with respect to fracture geometry and meshing. Hence, our coupled solution strategy represents a simple approach in terms of formulation, implementation and meshing. We demonstrate our model by some numerical examples on both synthetic and realistic problems, including a benchmark study for single-phase flow. Despite the simplicity of the method, the results are promising.

*Keywords:* Discrete fracture-matrix model, Embedded interface, Finite element method, Finite volume method, Porous media flow

---

## 1. Introduction

Modeling fluid flow in fractured porous media is an important yet challenging problem in subsurface engineering. Fractures are characterized as thin layers with either very high or low conductivity. They can therefore act as preferential paths or barriers and be essential to the fluid flow. The fracture width is typically several orders of magnitude smaller than any other characteristic sizes in the reservoir, and the flow rate can be orders of magnitude larger or smaller than in the surrounding matrix. This pose great challenges to the fracture model and the numerical method.

In this work we consider a discrete fracture-matrix (DFM) model, where the fractures are modeled as lower dimensional interfaces embedded in the rock matrix. We assume Darcy flow both in the matrix and the fracture, and we only consider the case where the permeability in the fractures are orders of magnitude larger than in the matrix. As flow model we consider incompressible single-phase flow governed by conservation of mass and Darcy's law. The flow problem is then coupled to a transport problem for a passive solute.

A common strategy to represent fractures in a DFM model is by averaging the governing equations across the fractures. The fracture width is then modeled as a coefficient in the equations rather than a geometrical property, and suitable coupling conditions between the fracture and matrix equations are applied. Common terminologies for such approximations are mixed-dimensional, hybrid-dimensional or reduced models. A

---

\*Corresponding author

Email address: lars.odsater@gmail.com (Lars H. Odsæter)

method for the high permeability case was presented in [2, 1], where the flow equations on mixed form are averaged over the interface assuming a continuous pressure. This model was later generalized by [17] and [32] to also handle the low permeability case, where a Robin type condition on the pressure at the interface is enforced. More recent DFM models similar to [17, 32] can be found in, e.g., [4, 21, 20, 41, 18, 8].

To account for more general fracture shapes, the model in [2, 1] was extended to curved fractures in [35, 14]. These models are derived by considering the asymptotic limit in the weak formulation as the fracture width tends to zero and the fracture permeability tends to infinity. In this limit, the condition of a continuous pressure follows. We mention that this model was extended to allow for pressure jumps across the interface in [14].

An embedded finite element method (EFEM) for the model in [14] was derived in [11]. Fractures are allowed to cut through the elements arbitrarily, and the fracture solution is represented by the restriction of the basis functions for the higher dimensional matrix elements. Contributions from the fracture to the fluid flow is included by superposition. A great advantage of this method is that it handles very general fracture geometry, including curved interfaces, bifurcations and intersections, and it is also easy to implement. The assumption of a continuous pressure along the fracture interface is a key ingredient as it allows for continuous elements. However, the normal flux is discontinuous across the fracture interface leading to loss of regularity, which can be resolved by local refinement close to the fractures based on an a priori error estimate. In this work, we apply EFEM for the pressure problem.

For the family of lower dimensional DFM models where the pressure is not assumed to be continuous, a great variety of numerical methods are suggested. We mention for instance finite element methods [28, 32, 3], finite volume methods [4, 9, 29], discontinuous Galerkin methods [5], mimetic finite difference methods [6, 42] and virtual element methods [22], all of which require a conforming mesh across the fracture interface. Different schemes with mortar coupling that allows for non-conforming meshes are presented in, e.g., [21, 8], but still the mesh needs to explicitly represent the fractures. Fully non-conforming discretizations have been realized through extended finite elements [15, 26, 41, 14].

The embedded DFM (EDFM) introduced by [31] is another approach where the fractures are allowed to cut arbitrarily through the higher dimensional mesh, see also [25, 34, 40, 39, 16] for newer contributions. EDFM is based on the two-point flux approximation (TPFA) where the fracture-fracture and fracture-matrix transmissibilities are approximated from geometrical quantities. Similar to EFEM, they are only valid for high permeability fractures, but the recently introduced projection-based EDFM (pEDFM) [44, 27] are also able to handle low permeability fractures. An important difference to EFEM is that the fractures are represented by their own lower dimensional elements along the fracture interface.

A comprehensive comparison of several DFM models for single-phase flow was conducted in a recent benchmark study [19]. We follow up on this study and evaluate EFEM on a selection of these benchmark problems.

The transport problem is also modeled by a reduced (or mixed-dimensional) model, see e.g., [1, 23, 22], where a coupling term models flow between the fracture and the matrix. We assume advection dominated flow since we are primarily interested in the coupling with the flow problem. In this work we present a novel discretization that is compatible with EFEM in the sense that the same computational mesh can be applied. This ensures that we have the same flexibility in terms of fracture geometry and meshing for the coupled solution strategy as is the case for EFEM. More specifically, we apply a low order upwind finite volume method (FVM), where the fracture solution is represented by elements cut by the fracture, and where the coupling term is approximated in a non-standard way by evaluating the normal velocity (flux) on the boundary of such elements. We mention here that an alternative approach is to use the CutFEM technology, see [12] for a stationary convection problem and [10] for a general introduction to CutFEM. For compatibility of the numerical solvers, we must require the velocity approximation from the flow problem to be locally conservative. This is not directly obtained by EFEM, but is achieved through a postprocessing step [37].

We mention that combining FEM and FVM for heterogeneous and fractured porous media have been studied before, e.g., the finite element–finite volume method [24, 38], where FEM is used for the flow problem and a node-centered finite volume method is used for transport. This method was extended in [36] to allow for a discontinuous solution across interfaces for the transport problem. However, this approach requires

fractures to me aligned with element boundaries and uses a dual mesh for the transport solver.

This paper is organized as follows. In Section 2 we describe the discrete fracture-matrix models and the governing equations for the coupled flow and transport problem. Next, in Section 3, we define the numerical methods. This includes EFEM for the flow problem, FVM for the transport problem, and the velocity approximation which couples the two subproblems. In Section 4 some numerical results are presented, including a realistic problem with a complex fracture network. Finally, we make some concluding remarks in Section 5.

## 2. Model formulation

As model problem we consider incompressible single-phase flow with advective transport of a concentration in a fractured porous media. Let  $\Omega \in \mathbb{R}^d$ , with  $d = 2, 3$ , be a convex polygonal domain with an embedded interface  $\Gamma$  representing the fractures. The bulk domain  $\Omega \setminus \Gamma$  will be referred to as the matrix. We denote by  $\boldsymbol{\kappa}$  and  $\phi$  the symmetric positive definite permeability tensor and porosity of the matrix, respectively. The fracture permeability is assumed to be isotropic and is denoted  $\kappa_\Gamma$ . We denote by  $w$  and  $\phi_\Gamma$  the fracture aperture and the porosity of the fractures, respectively. Moreover,  $k_\Gamma = w\kappa_\Gamma$  is the effective (scaled by fracture aperture) fracture permeability. Next,  $q$  and  $q_\Gamma$  denotes source or sink terms in the matrix and fractures, respectively. The primary unknowns are the fluid pressure  $p$ , from which we can derive the fluid velocity  $\mathbf{u}$ , and the concentration  $c$ .

For the flow problem, the boundary  $\partial\Omega$  is partitioned into a Dirichlet and Neumann part, denoted  $\partial\Omega_D$  and  $\partial\Omega_N$ , respectively. For the transport problem, we let  $\partial\Omega_{\text{in}} := \{\mathbf{x} \in \partial\Omega | \mathbf{u} \cdot \mathbf{n} < 0\}$  denote the inflow boundary, and  $\partial\Omega_{\text{out}} := \{\mathbf{x} \in \partial\Omega | \mathbf{u} \cdot \mathbf{n} \geq 0\}$  denote the outflow boundary, where  $\mathbf{n}$  is the outward pointing unit normal.

We use the standard notation  $H^s(\omega)$  for the Sobolev space of order  $s$  on  $\omega$  with the special cases  $L^2(\omega) = H^0(\omega)$  and  $H_0^1(\Omega) = \{v \in H^1(\Omega) : v|_{\partial\Omega_D} = 0\}$ . The space of continuous functions on  $\omega$  is denoted  $C(\omega)$ . For a normed vector space  $V$ , we let  $\|\cdot\|_V$  denote the norm on  $V$ . For  $V = L^2(\omega)$ , we use the notation  $\|\cdot\|_{L^2(\omega)} = \|\cdot\|_\omega$ , and denote by  $(\cdot, \cdot)_\omega$  the  $L^2$  scalar product.

In the following, we restrict this presentation to the two dimensional case, i.e.,  $d = 2$ , but most of the theory and methods considered herein can be extended to three dimensions in a straight forward manner.

### 2.1. Fracture representation

We allow for bifurcating fractures and represent  $\Gamma$  as a graph with nodes  $\mathcal{N} = \{\mathbf{x}_i\}_{i \in I_N}$  and edges  $\mathcal{G} = \{\Gamma_j\}_{j \in I_G}$ , where  $I_N$  and  $I_G$  are finite index sets, and each  $\Gamma_j$  is a curve between two nodes with indices  $I_N(j)$ . For each  $i \in I_N$ , we let  $I_G(i)$  be the set of indices corresponding to curves for which  $\mathbf{x}_i$  is an end point. Furthermore, let  $\{\Omega_i\}_{i=1}^{n_d}$  be a partition of  $\Omega$  into  $n_d$  subdomains defined by  $\Gamma$ . See Fig. 1a.

We fix an orientation of each  $\Gamma_j$  such that the positive direction is from the node with lowest index towards the node with highest index. Then we define  $\mathbf{n}_\Gamma$  to be the unit normal on  $\Gamma$  pointing from the left side towards the right when facing the positive direction of  $\Gamma$ , see Fig 1b. For a scalar function  $v$ , possibly discontinuous at  $\Gamma$ , we define the jump as

$$[[v]] = v_+ - v_-, \quad \text{on } \Gamma, \quad (2.1)$$

where

$$v_+(\mathbf{x}) = \lim_{\epsilon \rightarrow 0^+} v(\mathbf{x} + \epsilon \mathbf{n}_\Gamma), \quad \mathbf{x} \in \Gamma, \quad (2.2)$$

$$v_-(\mathbf{x}) = \lim_{\epsilon \rightarrow 0^+} v(\mathbf{x} - \epsilon \mathbf{n}_\Gamma), \quad \mathbf{x} \in \Gamma. \quad (2.3)$$

For a vector valued function  $\mathbf{v}$ , we define the jump in the normal component across  $\Gamma$  as

$$[[\mathbf{v} \cdot \mathbf{n}]] = \mathbf{v}_+ \cdot \mathbf{n}_+ + \mathbf{v}_- \cdot \mathbf{n}_-, \quad (2.4)$$

where  $\mathbf{n}_+ = -\mathbf{n}_\Gamma$  and  $\mathbf{n}_- = \mathbf{n}_\Gamma$ .

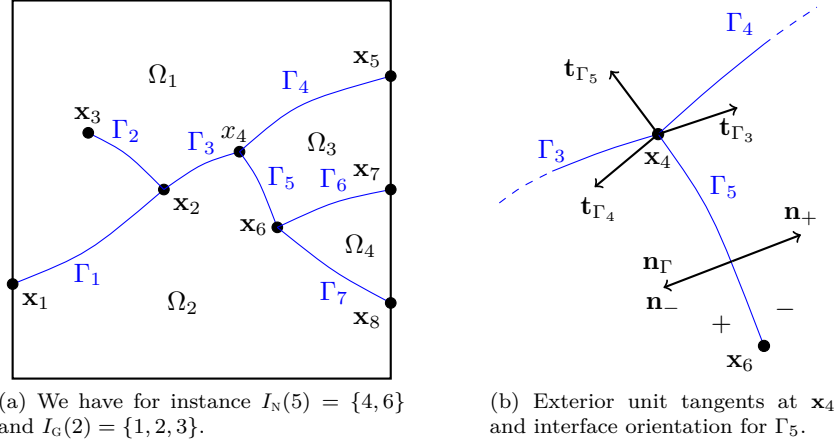


Figure 1: Illustration of domain and fracture representation.

## 2.2. Pressure problem

The fractures are modeled as embedded surfaces with high permeability. Our model is essentially the same as the one presented in [1, 14]. It was further studied in [11], where it was extended to bifurcating fractures. The embedded model is derived as the asymptotic limit in the weak formulation as the fracture aperture goes to zero and the fracture permeability goes to infinity. We refer to [1, 14] for further details.

*Boundary value problem.* The governing equations for the pressure problem are

$$-\nabla \cdot (\boldsymbol{\kappa} \nabla p) = q, \quad \text{in } \Omega, \quad (2.5a)$$

$$-\nabla_\Gamma \cdot (k_\Gamma \nabla_\Gamma p) = q_\Gamma + \llbracket (\boldsymbol{\kappa} \nabla p) \cdot \mathbf{n} \rrbracket, \quad \text{on } \Gamma, \quad (2.5b)$$

$$\llbracket p \rrbracket = 0, \quad \text{on } \Gamma, \quad (2.5c)$$

where  $\nabla_\Gamma = \mathbf{P} \nabla$  is the tangential gradient with  $\mathbf{P} = \mathbf{I} - \mathbf{n}_\Gamma \otimes \mathbf{n}_\Gamma$ . The first equation (2.5a) is the standard Darcy equation for single-phase flow describing conservation of mass. Eq. (2.5b) governs conservation of mass in the fractures, where the last term on the right hand side represents a coupling term for the normal velocity across  $\Gamma$ . The last equation (2.5c) is another coupling term, and represents a reasonable assumption for high conductive fractures. The model can also be extended to a non-zero pressure jump [14].

**Remark 2.1.** *Since we assume the pressure  $p$  to be continuous across  $\Gamma$  we will not use different notation for the pressure in the fracture and in the matrix. For other lower dimensional discrete fracture-matrix models where the pressure in the fracture is represented by its own variable, e.g. [17, 32], such distinction would be appropriate. In the following derivation, we will however let  $p_{\Gamma_j}$  refer to the pressure in the fracture segment  $\Gamma_j \subseteq \Gamma$ , for  $j \in I_G$ , but such terms will not appear in the weak formulation due to continuity conditions.*

We equip the governing equations with Dirichlet and Neumann boundary conditions, i.e.,

$$p = p_D, \quad \text{on } \partial\Omega_D, \quad (2.5d)$$

$$(\boldsymbol{\kappa} \nabla p) \cdot \mathbf{n} = u_N, \quad \text{on } \partial\Omega_N. \quad (2.5e)$$

Furthermore, we enforce continuity of pressure at the interface nodes,

$$p_{\Gamma_k}(x_i) = p_{\Gamma_l}(x_i), \quad \forall k, l \in I_G(i), \forall i \in I_N, \quad (2.5f)$$

and apply the Kirchhoff condition

$$\sum_{j \in I_G(i)} ((k_{\Gamma_j} \nabla_{\Gamma_j} p_{\Gamma_j}) \cdot \mathbf{t}_{\Gamma_j})|_{x_i} = 0, \quad \forall i \in I_N \setminus I_{N,N}, \quad (2.5g)$$

$$((k_{\Gamma_j} \nabla_{\Gamma_j} p_{\Gamma_j}) \cdot \mathbf{t}_{\Gamma_j})|_{x_i} = w u_N, \quad \forall i \in I_{N,N}, \quad (2.5h)$$

where  $\mathbf{t}_{\Gamma_j}$  is the exterior unit tangent to  $\Gamma_j$  (see Fig. 1b) and  $I_{N,N} \subset I_N$  is the set of indices whose corresponding nodes belong to  $\partial\Omega_N$ . We remark that Eq. (2.5g) ensures mass balance at the interface nodes, while Eq. (2.5h) is a Neumann condition for the part of  $\Gamma$  that intersects with  $\partial\Omega_N$ , and where the fracture width  $w$  is taken into account. Observe that Eq. (2.5g) implies a homogeneous Neumann condition at the fracture tip if the tip is in the interior of  $\Omega$ . This is a natural approximation that is commonly used, see e.g., [4, 21, 20, 8].

The fluid velocity is defined by Darcy's law as  $\mathbf{u} = -\boldsymbol{\kappa}\nabla p$ . We note that  $\mathbf{u}_\Gamma = -k_\Gamma\nabla_\Gamma p$  gives the flow rate through the cross section of the fracture rather than the velocity.

*Weak formulation.* We define the following function spaces,

$$V_\Gamma(\Gamma) = \{v \in C(\Gamma) : v \in H^1(\Gamma_j), \forall j \in I_G\}, \quad (2.6)$$

$$V_0(\Omega) = \{v \in H_0^1(\Omega) : v|_\Gamma \in V_\Gamma(\Gamma)\}, \quad (2.7)$$

$$V_D(\Omega; v_D) = \{v \in H^1(\Omega) : v|_{\partial\Omega_D} = v_D, v|_\Gamma \in V_\Gamma(\Gamma)\}. \quad (2.8)$$

Then multiply (2.5a) by a test function  $v \in V_0(\Omega)$ , integrate over  $\Omega$  and apply Green's formula on each subdomain  $\Omega_i$ , to obtain

$$\begin{aligned} (q, v)_\Omega &= \sum_{i=1}^{n_d} (-\nabla \cdot (\boldsymbol{\kappa}\nabla p), v)_{\Omega_i} \\ &= \sum_{i=1}^{n_d} ((\boldsymbol{\kappa}\nabla p, \nabla v)_{\Omega_i} - ((\boldsymbol{\kappa}\nabla p) \cdot \mathbf{n}_i, v)_{\partial\Omega_i}) \\ &= (\boldsymbol{\kappa}\nabla p, \nabla v)_\Omega - (\llbracket (\boldsymbol{\kappa}\nabla p) \cdot \mathbf{n} \rrbracket, v)_\Gamma - (u_N, v)_{\partial\Omega_N} \\ &= (\boldsymbol{\kappa}\nabla p, \nabla v)_\Omega - (q_\Gamma, v)_\Gamma - (\nabla_\Gamma \cdot (k_\Gamma \nabla_\Gamma p), v)_\Gamma - (u_N, v)_{\partial\Omega_N}. \end{aligned} \quad (2.9)$$

Notice that  $\mathbf{n}_i$  denotes the unit normal pointing out of  $\Omega_i$ . Then apply Green's formula on  $\Gamma$  and use the Kirchoff conditions, Eq. (2.5g)–(2.5h), to obtain

$$\begin{aligned} -(\nabla_\Gamma \cdot (k_\Gamma \nabla_\Gamma p), v)_\Gamma &= \sum_{j \in I_G} -(\nabla_{\Gamma_j} \cdot (k_{\Gamma_j} \nabla_{\Gamma_j} p_{\Gamma_j}), v)_{\Gamma_j} \\ &= \sum_{j \in I_G} (k_{\Gamma_j} \nabla_{\Gamma_j} p_{\Gamma_j}, \nabla_{\Gamma_j} v)_{\Gamma_j} - \sum_{j \in I_G} \sum_{i \in I_N(j)} ((k_{\Gamma_j} \nabla_{\Gamma_j} p_{\Gamma_j}) \cdot \mathbf{t}_{\Gamma_j}, v)_{x_i} \\ &= (k_\Gamma \nabla_\Gamma p, \nabla v)_\Gamma - \sum_{i \in I_N} \sum_{j \in I_G(i)} ((k_{\Gamma_j} \nabla_{\Gamma_j} p_{\Gamma_j}) \cdot \mathbf{t}_{\Gamma_j})|_{x_i} v(x_i) \\ &= (k_\Gamma \nabla_\Gamma p, \nabla v)_\Gamma - \sum_{i \in I_{N,N}} w u_N(x_i) v(x_i). \end{aligned} \quad (2.10)$$

Combing these equations we get the following weak formulation. Find  $p \in V_D(\Omega; p_D)$  such that

$$a(p, v) = l(v), \quad \forall v \in V_0(\Omega), \quad (2.11)$$

where

$$a(u, v) = (\boldsymbol{\kappa}\nabla u, \nabla v)_\Omega + (k_\Gamma \nabla_\Gamma u, \nabla v)_\Gamma, \quad (2.12)$$

$$l(v) = (q, v)_\Omega + (q_\Gamma, v)_\Gamma - (u_N, v)_{\partial\Omega_N} - \sum_{i \in I_{N,N}} w u_N(x_i) v(x_i). \quad (2.13)$$

Observe that the contribution from the fractures are included by superposition, i.e., by evaluating lower dimensional integrals along  $\Gamma$ .

**Remark 2.2.** When applying Green's formula in Eq. (2.9), we assume that there are no interfaces  $\Gamma_j$  that terminates in the interior of  $\Omega$  (as is the case for  $\Gamma_2$  in Fig. 1a). In such cases we can divide in two the domains  $\Omega_i$  with a terminating node such that the two new domains, denoted  $\Omega_{ia}$  and  $\Omega_{ib}$ , are separated by the interface with the terminating node and an artificial line connecting the terminating node with either  $\partial\Omega$  or another interface. We can then replace the contribution from  $\Omega_i$  by the sum of the contributions from  $\Omega_{ia}$  and  $\Omega_{ib}$  in Eq. (2.9). For the situation in Fig. 1a, we may for instance divide  $\Omega_1$  into two subdomains,  $\Omega_{1a}$  and  $\Omega_{1b}$ , separated by  $\Gamma_2$  and a line connecting  $\mathbf{x}_3$  with the upper left corner of  $\Omega$ . We mention that a similar approach was used in [4].

### 2.3. Transport problem

Advective transport in the fractured domain is modeled by a reduced (or mixed-dimensional) model, see e.g., [1, 23, 22],

$$\phi \frac{\partial c}{\partial t} + \nabla \cdot (\mathbf{u}c) = f(c), \quad \text{in } \Omega \times (0, T], \quad (2.14a)$$

$$w\phi_\Gamma \frac{\partial c_\Gamma}{\partial t} + \nabla_\Gamma \cdot (\mathbf{u}_\Gamma c_\Gamma) - \llbracket \mathbf{u} \cdot \mathbf{n}c^* \rrbracket = f_\Gamma(c_\Gamma), \quad \text{in } \Gamma \times (0, T], \quad (2.14b)$$

Initial and boundary conditions are given as

$$c = c_0, \quad \text{on } \Omega \times \{0\}, \quad (2.14c)$$

$$c_\Gamma = c_{\Gamma,0}, \quad \text{on } \Gamma \times \{0\}, \quad (2.14d)$$

$$c = c_B, \quad \text{on } \partial\Omega_{\text{in}} \times (0, T], \quad (2.14e)$$

$$c_\Gamma = c_{\Gamma,B}, \quad \text{on } \Gamma_{\text{in}} \times (0, T]. \quad (2.14f)$$

Here  $c_0$  and  $c_{\Gamma,0}$  are the initial concentrations in the matrix and fractures, respectively, while  $c_B$  and  $c_{\Gamma,B}$  are the inflow concentrations for the matrix and fractures, respectively. The right hand sides denote source terms, defined as

$$f(c) = \check{q}c + \hat{q}c_w = \begin{cases} qc, & \text{if } q \leq 0, \\ qc_w, & \text{if } q > 0, \end{cases} \quad (2.15a)$$

$$f_\Gamma(c_\Gamma) = \check{q}_\Gamma c_\Gamma + \hat{q}_\Gamma c_w = \begin{cases} q_\Gamma c_\Gamma, & \text{if } q_\Gamma \leq 0, \\ q_\Gamma c_w, & \text{if } q_\Gamma > 0, \end{cases} \quad (2.15b)$$

where  $\check{q} = \min(q, 0)$  and  $\hat{q} = \max(q, 0)$ , and  $c_w$  is the inflow concentration from the source term. The third term in the fracture equation (2.14b),  $\llbracket \mathbf{u} \cdot \mathbf{n}c^* \rrbracket$ , is a coupling term that models flow between the fracture and matrix. Here,  $c^*$  is interpreted as

$$c_\pm^* = \begin{cases} c_\pm, & \text{if } (\mathbf{u} \cdot \mathbf{n})_\pm \geq 0, \\ c_\Gamma, & \text{otherwise,} \end{cases} \quad \text{on } \Gamma \times (0, T]. \quad (2.16)$$

Observe that the transport problem is coupled to the pressure problem through the velocities  $\mathbf{u}$  and  $\mathbf{u}_\Gamma$ .

## 3. Numerical methods

### 3.1. Preliminaries

*Domain discretization.* Let  $\mathcal{K}_h$  be a partition of  $\Omega$ , and denote by  $K \in \mathcal{K}_h$  an element of the partition. We let  $K \in \mathcal{K}_h$  be open such that  $\bigcup_{K \in \mathcal{K}_h} \bar{K} = \bar{\Omega}$ . The diameter of  $K$  is denoted  $h_K$ , while  $h$  is the maximum diameter of all elements. We assume  $\mathcal{K}_h$  to be regular and quasi-uniform. By regular we mean that all elements are convex and that there exists  $\rho > 0$  such that each element  $K \in \mathcal{K}_h$  contains a ball of radius

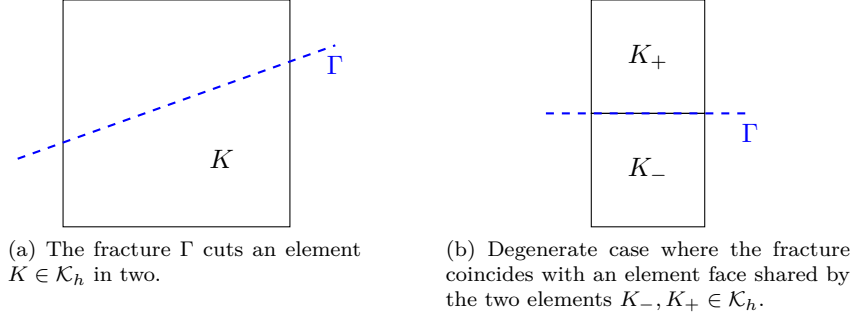


Figure 2: Fracture and element intersection.

$\rho h_K$  in its interior. Furthermore,  $\mathcal{K}_h$  is quasi-uniform if there exists  $\tau > 0$  such that  $h/h_K \leq \tau$  for all  $K \in \mathcal{K}_h$ . The fracture  $\Gamma$  is allowed to cut through the elements arbitrarily, see Fig. 2.

We denote by  $\mathcal{F}_h$  the set of all element faces. This set is then divided into the set of interior faces,  $\mathcal{F}_{h,I}$ , and boundary faces,  $\mathcal{F}_{h,B}$ . We assume that each face in  $\mathcal{F}_{h,B}$  is either completely on the Dirichlet or Neumann part of the boundary, such that  $\mathcal{F}_{h,B}$  can be split into  $\mathcal{F}_{h,D}$  and  $\mathcal{F}_{h,N}$ , i.e., the sets of faces on the Dirichlet and Neumann boundary, respectively. Similarly, let  $\mathcal{F}_{h,in}$  and  $\mathcal{F}_{h,out}$  be the set of boundary faces on the inflow and outflow boundary, respectively. For each face  $F \in \mathcal{F}_h$  we choose an orientation and let  $\mathbf{n}_F$  denote the unit normal in this direction. The unit normal vector on  $F \in \mathcal{F}_{h,B}$  is chosen to coincide with the outward unit normal. Furthermore,  $\mathbf{n}_K$  denotes the unit normal pointing out of  $K$ . We will also use the notation  $|K|$  for the measure of  $K$ , and similarly  $|F|$  for the measure of  $F$ .

For the transport solver, we further divide  $\mathcal{K}_h$  into two subsets,  $\mathcal{K}_h^M$  and  $\mathcal{K}_h^F$ , where  $\mathcal{K}_h^F$  contains all fractured cells,  $\mathcal{K}_h^F = \{K \in \mathcal{K}_h : K \cap \Gamma \neq \emptyset\}$ , and  $\mathcal{K}_h^M = \mathcal{K}_h \setminus \mathcal{K}_h^F$ , see Fig. 3a. The set of interior faces,  $\mathcal{F}_{h,I}$  are then partitioned into three subsets,  $\mathcal{F}_{h,I}^F$ ,  $\mathcal{F}_{h,I}^M$  and  $\mathcal{F}_{h,I}^{FM}$ , where  $\mathcal{F}_{h,I}^F$  are the set of faces between two fractured elements,  $\mathcal{F}_{h,I}^M$  is the set of faces between two matrix elements, and  $\mathcal{F}_{h,I}^{FM}$  are the sets of faces between a fracture and a matrix element.

**Remark 3.1.** *In the situation where  $\Gamma$  coincides with an element face  $F = \partial K_- \cap \partial K_+ \in \mathcal{F}_{h,I}$  as depicted in Fig. 2b, we need to choose which of the neighboring elements belong to  $\mathcal{K}_h^F$ . One possibility is to choose the element for which  $\mathbf{n}_\Gamma$  is exterior, i.e.,  $K_-$ . For the numerical examples presented in Section 4 we have avoided this situation.*

*Jump and average operators.* We define the jump operator  $[[\cdot]]$  over a face  $F \in \mathcal{F}_h$  in the same way as we did for the jump over  $\Gamma$ , see Eq. (2.1) and (2.4), where  $\mathbf{n}_F$  now defines the orientation. Furthermore, we denote by  $\{\{\cdot\}\}_\theta$  the weighted average operator on  $F$ , defined as

$$\{\{v\}\}_\theta = \theta_F v_- + (1 - \theta_F) v_+, \quad (3.1)$$

where  $\theta_F = \theta|_F$  and  $0 \leq \theta \leq 1$ . For  $\theta = \frac{1}{2}$  we simply write  $\{\{\cdot\}\}$  without any subscript. For  $F \in \mathcal{F}_{h,B}$  we define the jump and average operators as the one sided value, i.e.,

$$[[v]] = \{\{v\}\}_\theta = v_-. \quad (3.2)$$

*Finite dimensional function spaces.* In our implementation we work with quadrilateral elements, but the all numerical methods can equally well be formulated on other elements, e.g., triangular. Denote by  $\hat{K} = (0, 1)^2$  the reference element with coordinates  $(\xi, \eta)$ , and by  $M_K$  the mapping from  $\hat{K}$  to  $K$ . With this, we denote by  $\hat{Q}_r(\hat{K})$  the tensor product of polynomial spaces of degree less than or equal to  $r$  in each spatial direction, i.e.,

$$\hat{Q}_r(\hat{K}) = \left\{ v \in H^1(\hat{K}) : v = \left( \sum_{i=0}^r a_i \xi^i \right) \left( \sum_{i=0}^r b_i \eta^i \right), a_i, b_i \in \mathbb{R} \right\}. \quad (3.3)$$

Next,  $Q_r(K)$  denotes the reference element functions mapped to the actual element  $K$ ,

$$Q_r(K) = \{\hat{v} \circ M_K^{-1} : \hat{v} \in \hat{Q}_r(\hat{K})\}. \quad (3.4)$$

We may now define the following function spaces of piecewise polynomials of order  $r > 0$ ,

$$Q_r(\mathcal{K}_h) = \{v \in C(\Omega) : v|_K \in Q_r(K), K \in \mathcal{K}_h\}, \quad (3.5)$$

$$Q_{r,D}(\mathcal{K}_h; v_D) = \{v \in Q_r(\mathcal{K}_h) : v|_{\partial\Omega_D} = v_D\}. \quad (3.6)$$

Moreover, we define the following spaces of piecewise constant functions ( $r = 0$ ),

$$Q_0(\mathcal{K}_h) = \{v \in L^2(\Omega) : v|_K = a_K, a_K \in \mathbb{R}, K \in \mathcal{K}_h\}, \quad (3.7)$$

$$Q_0(\mathcal{F}_h) = \{v \in L^2(\mathcal{F}_h) : v|_F = a_F, a_F \in \mathbb{R}, F \in \mathcal{F}_h\}. \quad (3.8)$$

Finally, we denote by  $(\cdot, \cdot)_{\mathcal{K}_h}$  and  $(\cdot, \cdot)_{\mathcal{F}_h}$  the broken  $L^2$  scalar products, i.e.,

$$(u, v)_{\mathcal{K}_h} = \sum_{K \in \mathcal{K}_h} (u, v)_K, \quad (u, v)_{\mathcal{F}_h} = \sum_{F \in \mathcal{F}_h} (u, v)_F. \quad (3.9)$$

### 3.2. Pressure problem

We follow [11] and approximate the pressure solution with piecewise bilinear functions by restricting the weak formulation (2.11) to the finite dimensional subspace  $Q_{1,D}(\mathcal{K}_h; p_D) \subset V_D(\Omega; p_D)$ . Find  $p_h \in Q_{1,D}(\mathcal{K}_h; p_D)$  such that

$$a(p_h, v) = l(v), \quad \forall v \in Q_{1,D}(\mathcal{K}_h; 0). \quad (3.10)$$

The following a priori error estimate for the pressure approximation was proved in [11]. Let  $\mathcal{N}_h(K) \subset \mathcal{K}_h$  be the set of all elements which are node neighbors of  $K$ , and let  $h_\Gamma$  denote the mesh parameter in the vicinity of  $\Gamma$  such that  $h_K \leq h_\Gamma$  for all  $K \in \mathcal{N}_h(K)$ . Then it holds that

$$\|p - p_h\|_\Omega + \|p - p_h\|_\Gamma \lesssim (h_\Gamma + h^2) \left( \sum_{i=1}^{n_d} \|p\|_{H^2(\Omega_i)} \right) + h_\Gamma^2 \|p\|_{H^2(\Gamma)}. \quad (3.11)$$

As a consequence, one should refine locally around the fractures until  $h_\Gamma \sim h^2$  to obtain the optimal order of convergence in terms of  $h$ .

**Remark 3.2.** *The estimate (3.11) was proved in [11] for the simple geometry where  $\Gamma$  is a smooth embedded interface in the interior of  $\Omega$  without boundary. It can be extended to the case where  $\Gamma$  is represented as a graph. However, depending on the geometry of  $\Gamma$ , we may lose regularity of the solution in the bulk domain, for instance this is the case for terminating nodes in the interior of  $\Omega$ , e.g.,  $\mathbf{x}_2$  in Fig. 1a). Assuming that the solution in the bulk domain resides in  $H^s(\Omega)$ , for some  $s \in [1, 2]$ , we can show using similar techniques as in [11] that  $u_\Gamma \in H^{s+1/2}(\Gamma)$ . We must then replace the term  $(h_\Gamma + h^2)$  by  $(h_\Gamma + h^{2(s-1)})$ . We note that the condition  $h_\Gamma \sim h^2$  is stronger than  $h_\Gamma \lesssim h^{2(s-1)}$  and thus we always enforce  $h_\Gamma \sim h^2$  leading to convergence of order  $h^{2(s-1)}$ . Further improvement may be obtained by additional adaptive mesh refinement in the vicinity of endpoints and nonconvex corners.*

### 3.3. Transport problem

We approximate the concentration solution by piecewise constants  $c_h \in Q_0(\mathcal{K}_h)$ , and let  $c_h$  on  $\mathcal{K}_h^F$  represent the concentration in the fractures, and  $c_h$  on  $\mathcal{K}_h^M$  represent the concentration in the matrix. We use an upwind approximation of the concentration on element faces. The numerical scheme can be formulated as a low order finite volume method (FV), or equivalently as a zeroth order (piecewise constant) Discontinuous Galerkin method (DG). We only express the FV formulation here, and refer to Appendix A.1 for the DG formulation.

*FV formulation.* We integrate the matrix equation (2.14a) over  $K \in \mathcal{K}_h^M$  to obtain the integral formulation

$$\int_K \phi \frac{\partial c}{\partial t} + \int_{\partial K} \mathbf{u} \cdot \mathbf{n}_K c = \int_K f(c), \quad K \in \mathcal{K}_h^M. \quad (3.12)$$

Similarly, for  $K \in \mathcal{K}_h^F$ , we integrate the fracture equation (2.14a) over  $K \cap \Gamma$  to obtain

$$\int_{K \cap \Gamma} w \phi_\Gamma \frac{\partial c_\Gamma}{\partial t} + \int_{\partial(K \cap \Gamma)} \mathbf{u}_\Gamma \cdot \mathbf{n}_{K \cap \Gamma} c_\Gamma - \int_{K \cap \Gamma} \llbracket \mathbf{u} \cdot \mathbf{n} c^* \rrbracket = \int_{K \cap \Gamma} f_\Gamma(c_\Gamma), \quad K \in \mathcal{K}_h^F. \quad (3.13)$$

The lowest order finite volume method is then obtained by replacing  $c$  by  $c_h \in Q_0(\mathcal{K}_h)$ . We use an upwind approximation on  $\partial K$ , i.e.,

$$\mathbf{u} \cdot \mathbf{n}_K c_h|_{F=\partial K \cap \partial \tilde{K}} = \begin{cases} \mathbf{u} \cdot \mathbf{n}_K c_h|_K, & \text{if } \mathbf{u} \cdot \mathbf{n}_K \geq 0, \\ \mathbf{u} \cdot \mathbf{n}_K c_h|_{\tilde{K}}, & \text{if } \mathbf{u} \cdot \mathbf{n}_K < 0, \end{cases} \quad (3.14a)$$

where  $\tilde{K}$  is a neighbor element of  $K$ . If  $F \subset \partial K$  is a boundary face, we have

$$\mathbf{u} \cdot \mathbf{n}_K c_h|_{F=\partial K \cap \partial \Omega} = \begin{cases} \mathbf{u} \cdot \mathbf{n}_K c_h|_K, & \text{if } \mathbf{u} \cdot \mathbf{n}_K \geq 0, \\ \mathbf{u} \cdot \mathbf{n}_K c_B, & \text{if } \mathbf{u} \cdot \mathbf{n}_K < 0. \end{cases} \quad (3.14b)$$

An equivalent upwind approximation of  $c_h$  is used on  $\partial(K \cap \Gamma)$ .

Recall the definition of the vector valued jump in Eq. (2.4). The coupling term in Eq. (3.13), with  $c$  replaced by  $c_h$ , can be written as

$$\llbracket \mathbf{u} \cdot \mathbf{n} c_h^* \rrbracket = (\mathbf{u} \cdot \mathbf{n}_\Gamma c_h^*)_ - - (\mathbf{u} \cdot \mathbf{n}_\Gamma c_h^*)_ +, \quad \text{on } K \cap \Gamma. \quad (3.15)$$

Given a velocity approximation that is continuous in the interior of an element, we see that  $\llbracket \mathbf{u} \cdot \mathbf{n} c_h^* \rrbracket$  vanish as long as  $\Gamma$  is not aligned with the element faces. This would result in no coupling between the fracture and the matrix. To overcome this, we approximate the flow between matrix and fracture by evaluating  $(\mathbf{u} \cdot \mathbf{n}_\Gamma c_h^*)_ \pm$  on the part of the element boundary that borders to matrix elements, i.e.,

$$\int_{K \cap \Gamma} \llbracket \mathbf{u} \cdot \mathbf{n} c_h^* \rrbracket \approx \sum_{\tilde{K} \in \mathcal{K}_h^M} \int_{\partial \tilde{K} \cap \partial K} \mathbf{u} \cdot \mathbf{n}_K c_h, \quad (3.16)$$

where the upwind scheme (3.14) applies. Since  $c_h$  on  $K \in \mathcal{K}_h^F$  represents the approximation in the fracture, (3.16) is compatible with the condition (2.16). Given the low order method, the approximation (3.16) seems reasonable when combined with local refinement around  $\Gamma$ .

We apply the implicit Euler (IE) method as time integrator. For simplicity, we use constant time steps  $\Delta t$ , and let  $c_h^n$  denote the approximation at  $t = n\Delta t$ , with  $c_h^0 = Q_0 c_0$ , where  $Q_0$  is a projection operator from  $L^2(\Omega)$  to  $Q_0(\mathcal{K}_h)$ .

To sum up, the FV-IE scheme can be formulated as follows. Find  $c_h^{n+1} \in Q_0(\mathcal{K}_h)$  such that

$$\int_K \phi \frac{c_h^{n+1} - c_h^n}{\Delta t} + \int_{\partial K} \mathbf{u} \cdot \mathbf{n}_K c_h^{n+1} = \int_K f^{n+1}(c_h^{n+1}), \quad \forall K \in \mathcal{K}_h^M, \quad (3.17a)$$

$$\begin{aligned} \int_{K \cap \Gamma} w \phi_\Gamma \frac{c_h^{n+1} - c_h^n}{\Delta t} + \int_{\partial(K \cap \Gamma)} \mathbf{u}_\Gamma \cdot \mathbf{n}_{K \cap \Gamma} c_h^{n+1} - \sum_{\tilde{K} \in \mathcal{K}_h^M} \int_{\partial \tilde{K} \cap \partial K} \mathbf{u} \cdot \mathbf{n}_K c_h^{n+1} \\ = \int_{K \cap \Gamma} f_\Gamma^{n+1}(c_h^{n+1}), \quad \forall K \in \mathcal{K}_h^F. \end{aligned} \quad (3.17b)$$

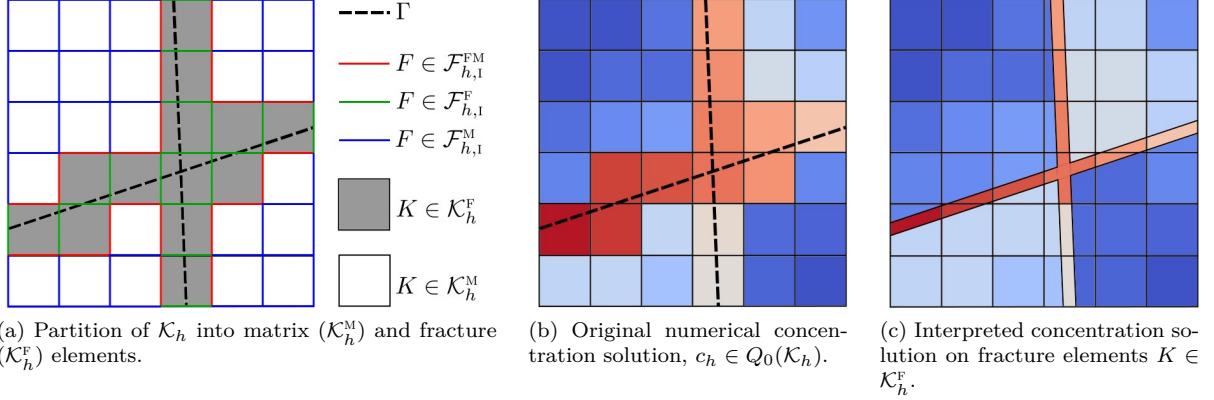


Figure 3: Synthetic example of partition into matrix and fracture elements, and corresponding interpretation of concentration solution. The interpreted solution on interface elements  $K \cap \Gamma$  is visualized with a fixed (exaggerated) thickness.

*Interpretation of solution.* In the numerical method,  $c|_{K \cap \Gamma}$ , for  $K \in \mathcal{K}_h^F$ , is represented by the value  $c_h|_K$ . However,  $K$  also contains subdomains belonging to the matrix, whose concentration solution we represent by the solution in the neighboring matrix elements, see Fig. 3 for an illustrative example. For a single fracture the matrix concentration in  $K$  to the left/right of  $\Gamma$  is given by the solution in the left/right-neighboring matrix elements. For cells  $K$  with intersecting or bifurcating fractures, this interpretation is slightly more complex, as  $\Gamma$  divides  $K$  into more than two subdomains. We refer to Appendix A.2 for a well-defined interpretation.

### 3.4. Velocity model

We observe from the transport model, Eq. (3.17), that we need the flux (normal velocity) over the element faces. We denote the flux by  $U$  and define it as

$$U = \begin{cases} -\kappa \nabla p \cdot \mathbf{n}_F, & \text{on } F \in \mathcal{F}_h \setminus (\mathcal{F}_{h,1}^F \cup \mathcal{F}_{h,N}), \\ -\frac{1}{|F|} k_\Gamma \nabla_\Gamma p \cdot \mathbf{t}_{\Gamma,F}, & \text{on } F \in \mathcal{F}_{h,1}^F, \\ u_N, & \text{on } F \in \mathcal{F}_{h,N}, \end{cases} \quad (3.18)$$

where  $\mathbf{t}_{\Gamma,F}$  is the unit tangent to  $\Gamma$  oriented in the same direction as  $\mathbf{n}_F$ . Recall that  $k_\Gamma = w\kappa_\Gamma$  so that  $k_\Gamma \nabla_\Gamma p \cdot \mathbf{t}_\Gamma$  gives the flow rate rather than the velocity. The reason for multiplying by  $1/|F|$  for faces  $F \in \mathcal{F}_{h,1}^F$  is that we want to work directly on  $\mathcal{F}_h$  so that when  $U$  is integrated over  $F$  we get the total flow rate through  $F$ . With this definition of  $U$  we can simplify two terms in Eq. (3.17b),

$$\int_{\partial(K \cap \Gamma)} \mathbf{u}_\Gamma \cdot \mathbf{n}_{K \cap \Gamma} c_h^{n+1} - \sum_{\tilde{K} \in \mathcal{K}_h^M} \int_{\partial \tilde{K} \cap \partial K} \mathbf{u} \cdot \mathbf{n}_K c_h^{n+1} = \int_{\partial K} U c_h^{n+1} \mathbf{n}_K \cdot \mathbf{n}_F. \quad (3.19)$$

The term  $\mathbf{n}_K \cdot \mathbf{n}_F$  is either plus or minus 1 depending on the orientation of  $F$ .

For the coupled flow and transport problem, the velocity is derived from the pressure approximation  $p_h$ . The pressure gradient,  $\nabla p_h$ , is not continuous across element faces, so a naive flux approximation is to use the average value,

$$U_h = \begin{cases} -\{\{\kappa \nabla p_h \cdot \mathbf{n}_F\}\}_\partial, & \text{on } F \in \mathcal{F}_h \setminus (\mathcal{F}_{h,1}^F \cup \mathcal{F}_{h,N}), \\ -\frac{1}{|F|} \{\{k_\Gamma \nabla_\Gamma p_h \cdot \mathbf{t}_\Gamma\}\}, & \text{on } F \in \mathcal{F}_{h,1}^F, \\ u_N, & \text{on } F \in \mathcal{F}_{h,N}. \end{cases} \quad (3.20)$$

Recall the definition of the average operator in Eq. (3.1). As weights we follow [37] and use weights equal to the normal component of the permeability of the neighboring cell. Hence,

$$\vartheta_F = \frac{\delta_{K_n}^+}{\delta_{K_n}^+ + \delta_{K_n}^-}, \quad \delta_{K_n}^\pm = \mathbf{n}_F \cdot (\boldsymbol{\kappa}_\pm \mathbf{n}_F), \quad (3.21)$$

where  $\boldsymbol{\kappa}_\pm$  are the permeabilities of the two cells sharing  $F$ . For a fractured cell we use  $\boldsymbol{\kappa} = \kappa_\Gamma \mathbf{I}$ , and for  $F \in \mathcal{F}_{h,b}$ ,  $\omega|_F = 1/\delta_{K_n}^-$ . In the case of isotropic permeability, i.e.,  $\boldsymbol{\kappa} = \kappa \mathbf{I}$ , observe that  $\vartheta_F = \kappa_+ / (\kappa_+ + \kappa_-)$  such that

$$U_h = -\{\{\boldsymbol{\kappa} \nabla p_h \cdot \mathbf{n}_F\}\}_\vartheta = -\frac{\kappa_+ \kappa_-}{\kappa_+ + \kappa_-} (\nabla p_h)_- \cdot \mathbf{n}_F - \frac{\kappa_- \kappa_+}{\kappa_+ + \kappa_-} (\nabla p_h)_+ \cdot \mathbf{n}_F = -k_e \{\{\nabla p_h \cdot \mathbf{n}_F\}\}, \quad (3.22)$$

where  $k_e = \frac{2\kappa_+ \kappa_-}{\kappa_+ + \kappa_-}$  is the effective face permeability (harmonic average).

We say that a flux approximation  $U_h$  on  $\mathcal{F}_h$  is locally conservative if

$$\int_{\partial K} U_h(\mathbf{n}_K \cdot \mathbf{n}_F) = \int_K q, \quad \forall K \in \mathcal{K}_h. \quad (3.23)$$

As reported in [37], Eq. (3.20) does not define a locally conservative flux approximation. If coupled to the transport scheme one may get unphysical solutions due to artificial sinks and sources. To deal with this, we apply the postprocessing method presented in [37]. This method was shown to preserve accuracy of the velocity solution and was demonstrated to be especially beneficial for highly heterogeneous media.

*Variationally consistent postprocessing of fluxes.* The core idea of the postprocessing method is to add a piecewise constant correction to  $U_h$  under the constraint that the correction is minimized in a weighted  $L^2$  norm,

$$\|v\|_{\omega, \mathcal{F}_h} = \sqrt{(\omega v, v)_{\mathcal{F}_h}}, \quad (3.24)$$

where  $\omega$  are positive and bounded weights. We define the weight on  $F \in \mathcal{F}_h$  as the inverse of the effective normal component of the permeability,

$$\omega|_F = \frac{\delta_{K_n}^+ + \delta_{K_n}^-}{2\delta_{K_n}^+ \delta_{K_n}^-}. \quad (3.25)$$

These weights were demonstrated to be a good choice for heterogeneous permeability as low permeable interfaces are better preserved compared to minimizing in the standard  $L^2$  norm ( $\omega = 1$ ) [37].

Next, we define a residual operator,  $\mathcal{R} : L^2(\mathcal{F}_h) \rightarrow Q_0(\mathcal{K}_h)$ , measuring the discrepancy from local conservation,

$$\mathcal{R}(U)|_K = \begin{cases} \frac{1}{|K|} \left( \int_K q - \int_{\partial K} U \mathbf{n}_F \cdot \mathbf{n}_K \right), & K \in \mathcal{K}_h^M, \\ \frac{1}{|K|} \left( \int_{K \cap \Gamma} q_\Gamma - \int_{\partial K} U \mathbf{n}_F \cdot \mathbf{n}_K \right), & K \in \mathcal{K}_h^F. \end{cases} \quad (3.26)$$

With this we define the postprocessed flux,  $V_h$ , as follows.

$$V_h = \begin{cases} U_h + \omega^{-1} \llbracket y \rrbracket, & \text{on } F \in \mathcal{F}_h \setminus \mathcal{F}_{h,N}, \\ u_N, & \text{on } F \in \mathcal{F}_{h,N}, \end{cases} \quad (3.27)$$

where  $y \in Q_0(\mathcal{K}_h)$  is the unique solution to

$$(\omega^{-1} \llbracket y \rrbracket, \llbracket w \rrbracket)_{\mathcal{F}_h \setminus \mathcal{F}_{h,N}} = (\mathcal{R}(U_h), w)_{\mathcal{K}_h}, \quad \forall w \in Q_0(\mathcal{K}_h). \quad (3.28)$$

Further details on the postprocessing method, including uniqueness and error analysis, are given in [30] and [37].

*Coupled formulation.* Applying Eq. (3.19) and using  $V_h$  as an approximation to  $U$ , the FV-IE scheme, Eq. (3.17), can be formulated as follows. Find  $c_h^{n+1} \in Q_0(\mathcal{K}_h)$  such that

$$\int_K \phi \frac{c_h^{n+1} - c_h^n}{\Delta t} + \int_{\partial K} V_h c_h^{n+1} \mathbf{n}_K \cdot \mathbf{n}_F = \int_K f^{n+1}(c_h^{n+1}), \quad \forall K \in \mathcal{K}_h^M, \quad (3.29a)$$

$$\int_{K \cap \Gamma} w \phi_\Gamma \frac{c_h^{n+1} - c_h^n}{\Delta t} + \int_{\partial K} V_h c_h^{n+1} \mathbf{n}_K \cdot \mathbf{n}_F = \int_{K \cap \Gamma} f_\Gamma^{n+1}(c_h^{n+1}), \quad \forall K \in \mathcal{K}_h^F. \quad (3.29b)$$

Note that the second term in Eq. (3.29b) contains both the flux along the fracture and the coupling term, cf. Eq. (3.19).

**Remark 3.3.** *In this contribution we focus on a low order method suitable for situations where the geometry of the domain is complicated, which is common in practical applications. The basic approach may be extended to higher order approximation but that requires the use of cut finite elements, see [12] and [13] for first steps in this direction, which leads to a significantly more complex implementation of the method. For low order approximations the simpler geometric modeling used in this paper is sufficient to achieve optimal order convergence. The postprocessing step is identical for higher order pressure approximations.*

**Remark 3.4.** *Since our model problem is one way coupled, i.e., the pressure is not dependent on the concentration, we typically first solve (3.10) for the pressure  $p_h$ , then we solve for the conservative flux  $V_h$  using (3.27) and (3.28), and finally we solve the time dependent transport problem for  $c_h^{n+1}$  given  $c_h^n$  by (3.29). If the problem is fully coupled, i.e., the pressure depends on the concentration, a monolithic solution procedure in each time step is an alternative. In that case we solve for all variables  $p_h^{n+1}$ ,  $V_h^{n+1}$ , and  $c_h^{n+1}$  in the same pass.*

## 4. Numerical results

In this section we validate the numerical methods presented in Section 3. First, in Section 4.1, we consider a pure transport problem where the velocity is given explicitly and the exact solution is known. This is to verify our transport model, Eq. (3.29), and in particular our approximation of the coupling term, see Eq. (3.16).

Next, in Section 4.2, we consider two benchmark cases for the pure pressure problem presented in [19]. The first case is a regular fracture network, while the second problem is a realistic case with a complex fracture network. The aim is to compare EFEM, Eq. (3.10), to other DFM models for single-phase flow.

Finally, in Section 4.3, we solve the coupled pressure and transport problem on the same cases as in Section 4.2. This will reveal the capabilities of our solution approach.

All computer implementation of the numerical methods are based on the open-source software deal.II [7] and are freely available under an open license<sup>1</sup>. We only consider 2D problems, but our fracture model and numerical methods can be applied to 3D problems as well. All meshes are built up of quadrilateral elements. The meshes may be locally refined by recursively dividing selected elements in four, but we allow for no more than one hanging node per element face. The number of degrees of freedom are denoted  $N_{\text{dof}}$ .

### 4.1. Pure transport problem

We consider first a pure transport problem with an explicitly given velocity field. Let  $\Omega = (0, 1)^2$  and  $\Gamma = (0, 1) \times \{0.5\}$ . The fracture velocity,  $u_\Gamma = \mathbf{u}_\Gamma \cdot (1, 0) = 10$ , and we consider two cases for the matrix velocity,  $\mathbf{u}$ . Either  $\mathbf{u} = (0, 1)$  for  $y < 0.5$  and  $\mathbf{u} = (0, -1)$  otherwise, or  $\mathbf{u} = (0, -1)$  for  $y < 0.5$  and  $\mathbf{u} = (0, 1)$  otherwise. The two cases are depicted in Fig. 4 and are denoted *inflow* and *outflow*, respectively. In both cases we set  $w = 1$  and use initial and boundary conditions  $c_0 = 0$  and  $c_B = 1$ .

<sup>1</sup><https://github.com/laods/efsim>

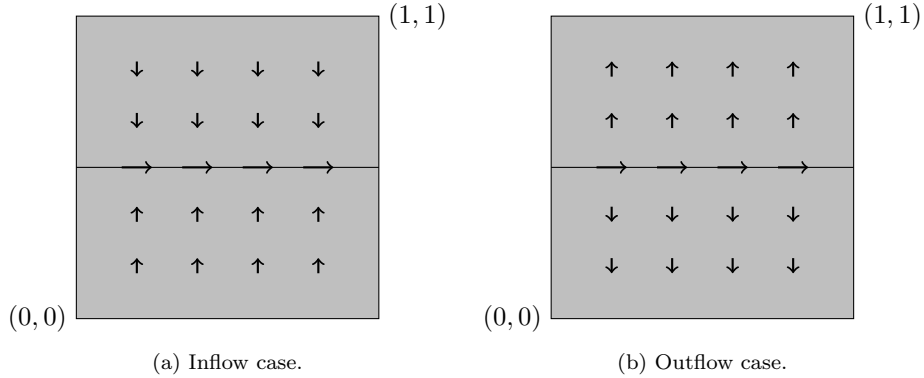


Figure 4: Pure transport problem: Description of the two cases. Arrows describe the velocity field.

The 1D advective transport equation describing the fracture concentration,  $c_\Gamma$ , is given as

$$w \frac{\partial c_\Gamma}{\partial t} + u_\Gamma \frac{\partial c_\Gamma}{\partial x} - \llbracket \mathbf{u} \cdot \mathbf{n} c^* \rrbracket = 0, \quad \text{on } \Gamma, \quad (4.1a)$$

$$c_\Gamma = 1, \quad \text{at } x = 0. \quad (4.1b)$$

For the inflow case we have  $c^* = c$ , and for the outflow case  $c^* = c_\Gamma$ . Both cases are solved on uniform  $N \times N$  meshes with time steps  $dt = 0.001$ , and the simulations are run until a steady-state solution is reached.

*Inflow case.* For the inflow case the concentration front from the top and bottom boundary moves with speed 1, so that  $\llbracket \mathbf{u} \cdot \mathbf{n} c^* \rrbracket = 2c$  with  $c = 0$  for  $t < 0.5$  and  $c = 1$  for  $t > 0.5$ . Hence, the exact solution for  $t < 0.5$  reads

$$c_\Gamma(x, t) = \begin{cases} 1, & x < \frac{u_\Gamma}{w} t, \\ 0, & x \geq \frac{u_\Gamma}{w} t. \end{cases} \quad (4.2)$$

At steady-state,  $c = 1$  in the matrix, and the exact steady-state solution is

$$c_\Gamma^{\text{ss}}(x) = 1 + \frac{2w}{u_\Gamma} x. \quad (4.3)$$

The approximation,  $c_h$ , along the fracture is plotted at  $t = 0.05$  and  $t = 1.5$  (steady-state) in Fig. 5 and compared to the exact solution.

*Outflow case.* For the outflow case,  $\llbracket \mathbf{u} \cdot \mathbf{n}_\Gamma c^* \rrbracket = -2c_\Gamma$ , so that the exact solution reads

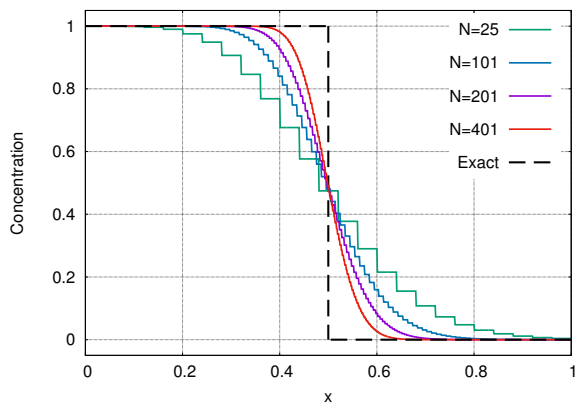
$$c_\Gamma(x, t) = \begin{cases} \exp\{-\frac{2}{u_\Gamma} x\}, & x < u_\Gamma t, \\ 0, & x \geq u_\Gamma t. \end{cases} \quad (4.4)$$

The approximation,  $c_h$ , along the fracture is plotted at  $t = 0.05$  and  $t = 1.5$  (steady-state) in Fig. 6 and compared to the exact solution.

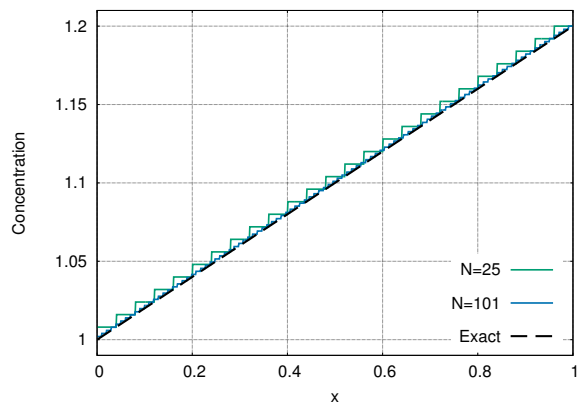
We observe that we get the correct steady-state solution in both cases, and that the velocity of the concentration front is correct. Due to the low order method we get significant numerical diffusion as expected, but we see that the front gets sharper as  $N$  increases.

#### 4.2. Benchmark cases for the pure pressure problem

In this section we consider two of the benchmark cases defined in [19] for the pure pressure problem. We only consider the cases where all fractures have higher permeability than the surrounding matrix as

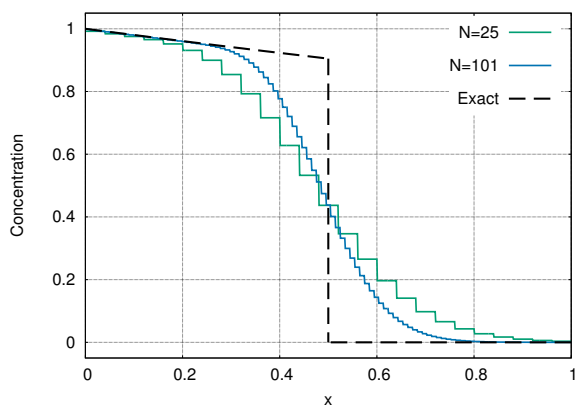


(a)  $t = 0.05$ .

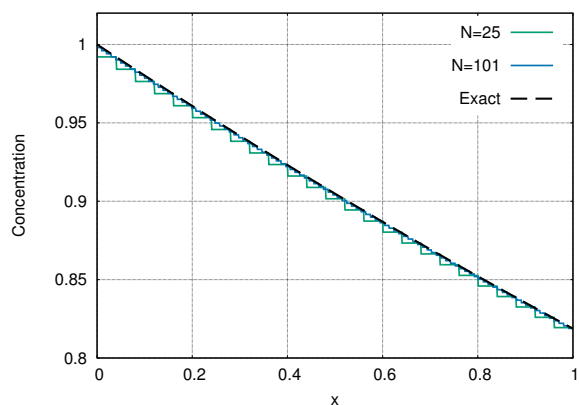


(b) Steady-state solution,  $t = 1.5$ .

Figure 5: Pure transport problem — inflow case: Fracture concentration on uniform  $N \times N$  meshes compared to exact solution.



(a)  $t = 0.05$ .



(b) Steady-state solution,  $t = 1.5$ .

Figure 6: Pure transport problem — outflow case: Fracture concentration on uniform  $N \times N$  meshes compared to exact solution.

Table 1: List of the participating methods in the benchmark paper [19].

Method	Description
Box	Vertex-centered finite-volume method
TPFA	Control volume finite difference method with two-point flux approximation
MPFA	Control volume finite difference method with multi-point flux approximation
EDFM	Embedded discrete fracture-matrix model
Flux-Mortar	Mortar discrete fracture-matrix model
P-XFEM	Primal extended finite element method
D-XFEM	Dual extended finite element method

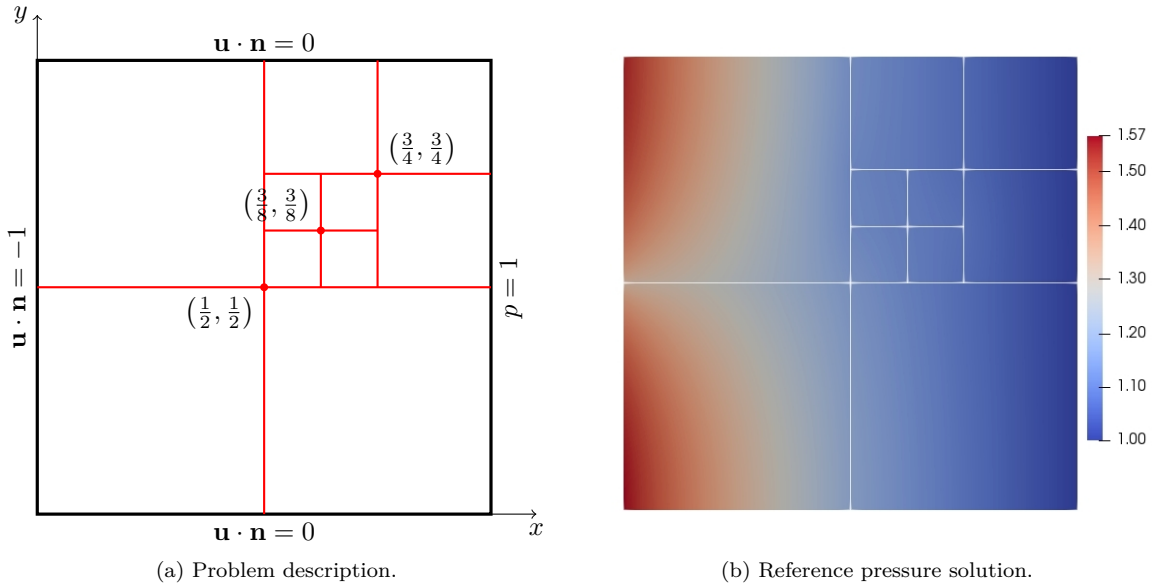


Figure 7: Benchmark 1 (pressure problem).

our model only applies to such problems. We employ the exact same problem setup as [19] and compare our results with those given therein<sup>2</sup>. The six methods considered in this study are listed in Table 1. We only give a very brief description of these methods here, and refer to [19] and references therein for further details. Our method will be denoted EFEM.

#### 4.2.1. Benchmark 1: Regular fracture network

Benchmark 1 is a regular fracture network embedded in the unit square,  $\Omega = (0, 1)^2$ , see Fig. 7a. The top and bottom boundary faces have homogeneous Neumann conditions (no flow); the left boundary face has a constant inflow flux,  $\mathbf{u} \cdot \mathbf{n} = -1$ ; and the right boundary face has Dirichlet condition  $p_D = 1$ . The rock properties are  $\boldsymbol{\kappa} = \mathbf{I}$ ,  $\kappa_\Gamma = 10^4$  and  $w = 10^{-4}$ .

A reference solution is obtained in [19] by using a mimetic finite difference (MFD) method on a very fine reference mesh where the fractures are resolved by 10 elements in their normal direction. The reference mesh is coarser away from the fractures and has a total of 1175056 elements. Hence, the fractures are not modeled as a lower dimensional embedding, but as a continuous model with  $\boldsymbol{\kappa} = \kappa_\Gamma \mathbf{I}$  in the fracture elements. We denote by  $K_{\text{ref}}$  the reference elements and by  $p_{\text{ref}}$  the reference solution. The reference solution is displayed in Fig. 7b.

<sup>2</sup>All results reported in [19] are public available at <https://git.iws.unistuttgart.de/benchmarks/fracture-flow>.

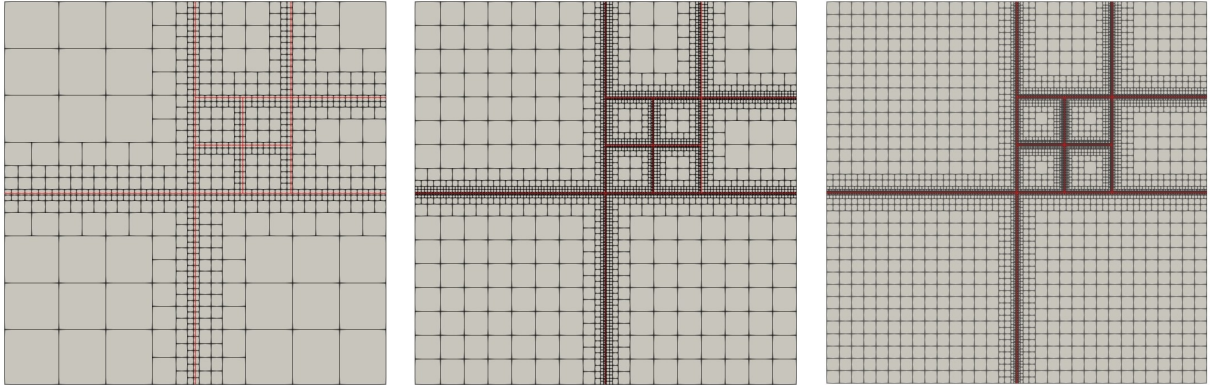


Figure 8: Benchmark 1 (pressure problem). Locally refined meshes with  $N_{\text{dof}}$  equal to 932, 4532 and 19579, respectively. Fractures are included as red lines. We avoid fractures along element faces.

To measure the error in the pressure solution, we define two error functions,  $err_M$  and  $err_F$ , measuring the error in the matrix and fractures, respectively,

$$err_M^2 = \frac{1}{|\Omega|(\Delta p_{\text{ref}})^2} \sum_{f=K_{\text{ref}} \cap K} |f|(p_h|_{f_m} - p_{\text{ref}}|_{K_{\text{ref}}})^2 \approx \frac{1}{|\Omega|(\Delta p_{\text{ref}})^2} \|p_h - p_{\text{ref}}\|_{L^2(\Omega)}^2, \quad (4.5)$$

$$err_F^2 = \frac{1}{|\Gamma|(\Delta p_{\text{ref}})^2} \sum_{e=(K_{\text{ref}} \cap K) \cap \Gamma} |e|(p_h|_{e_m} - p_{\text{ref}}|_{K_{\text{ref}}})^2 \approx \frac{1}{|\Gamma|(\Delta p_{\text{ref}})^2} \|p_h - p_{\text{ref}}\|_{L^2(\Gamma)}^2, \quad (4.6)$$

where  $\Delta p_{\text{ref}} = \max_{\Omega} p_{\text{ref}} - \min_{\Omega} p_{\text{ref}}$  and  $f_m$  and  $e_m$  denotes the midpoints of  $f$  and  $e$ , respectively. Observe that these are  $L^2$  errors where the integrals are approximated by the midpoint rule.

We solve the pressure problem on both uniform  $N \times N$  meshes with  $N = \{19, 37, 73, 139\}$ , denoted UMRN, and three locally refined meshes, denoted LR*i*, for  $i = 1, 2, 3$ , where the local refinement is based on the a priori estimate (3.11) such that  $h_{\Gamma} \lesssim h^2$  where  $h_{\Gamma}$  is the element size in the vicinity of the fractures. The LR meshes are shown in Fig. 8. The errors are plotted against  $N_{\text{dof}}$  in Fig. 9. We see that the error for the uniform meshes has convergence order  $N_{\text{dof}}^{-1/2}$  in accordance with the error estimate, while the error is lower and converge faster for the LR meshes.

In Table 2 we compare our results with the ones reported in [19], and we observe that the results are in good agreement. Furthermore, in Fig. 10 the pressure along the lines  $y = 0.7$  and  $x = 0.5$  are plotted, similarly to the results reported in [19]. We observe a good match with the reference solution, and in particular we see that the LR mesh gives better accuracy close to the fractures.

**Remark 4.1.** We would like to point out that the error functions in [19] are defined in a similar way, but instead of using  $p_h$  directly, the projection of  $p_h$  onto piecewise constant functions on the computational mesh is used. In the case where the pressure approximation is piecewise constant this is equivalent to what we do. However, for higher order polynomial approximations, the error functions used in [19] would give unfavorable results.

#### 4.2.2. Benchmark 4: A realistic case

We consider next benchmark 4 in [19]. The geometry represents a real set of fractures from an interpreted outcrop in the Sotra island, near Bergen in Norway, see [19] for more details. For this case  $\Omega = (0, 700) \times (0, 600)$  and  $\Gamma$  is the union of 64 straight fractures in a complex pattern, see Fig. 11. The matrix permeability is set to  $\kappa = 10^{-14} \mathbf{I} \text{ m}^2$ . All fractures have permeability  $\kappa_{\Gamma} = 10^{-8} \text{ m}^2$ , and aperture  $w = 10^{-2} \text{ m}$ . We apply homogeneous Neumann boundary conditions (no flow) on the top and bottom boundary faces,  $p_D = 1013250 \text{ Pa}$  on the left face, and  $p_D = 0 \text{ Pa}$  on the right face.

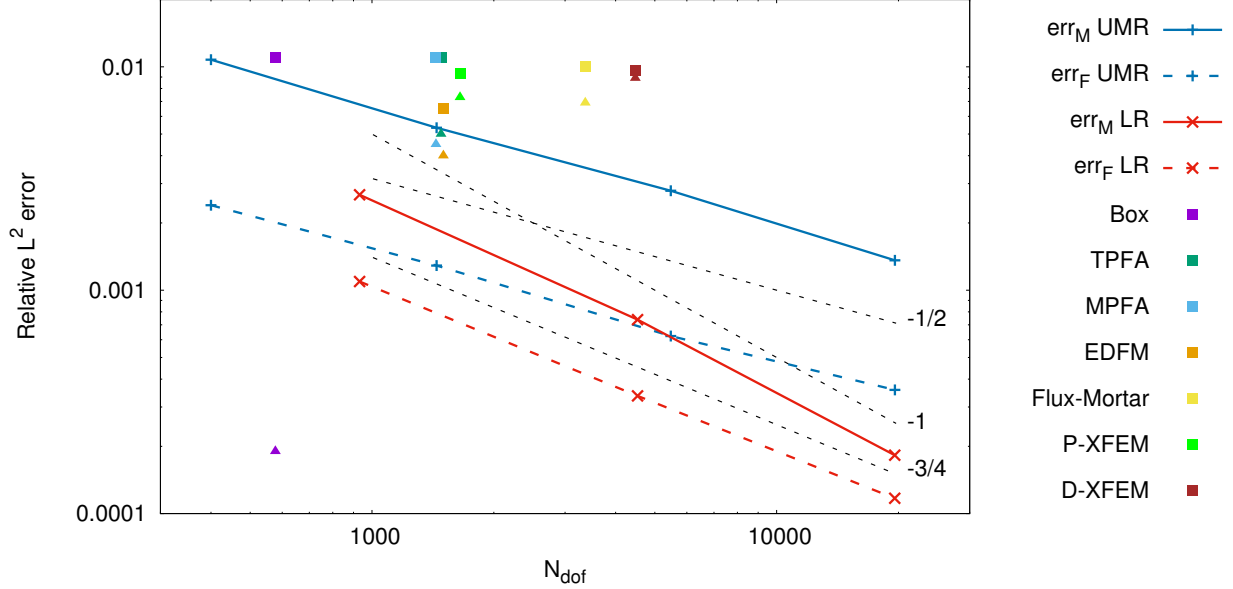


Figure 9: Benchmark 1 (pressure problem). Relative  $L^2$  errors,  $err_M$  and  $err_F$  (Eqs. (4.5) and (4.6)), plotted against degrees of freedom,  $N_{\text{dof}}$ . Solid lines denote the matrix error,  $err_M$ , and dashed lines denote the fracture error,  $err_F$ , for EFEM with UMR (blue) and LR (red) meshes. Black dotted lines are straight reference lines of labeled slope. Squares and triangles denote the errors for the methods reported in the benchmark paper [19] where squares represent  $err_M$  and triangles represent  $err_F$ . Each method is represented by its unique color according to the chart depicted to the right.

Table 2: Benchmark 1 (pressure problem). Comparison with the results in [19] for error, matrix density (nnz denotes number of non-zero entries in the system matrix) and matrix condition number. *No. of elements* for the methods in [19] are listed as matrix elements plus fracture elements. In light of Remark 4.1 we would like to point out that Box and EDFM have continuous pressure approximation, so that the errors associated with these would likely be smaller.

Method	$N_{\text{dof}}$	No. of elements	$err_M$	$err_F$	$\text{nnz}/N_{\text{dof}}^2$	$\ \cdot\ _2\text{-cond}$
EFEM UMR37	1444	1369	5.3e-3	1.3e-3	5.9e-3	3.3e4
EFEM LR1	932	757	2.7e-3	1.1e-3	7.0e-3	1.1e4
Box	577	1078 + 74	1.1e-2	1.9e-4	1.1e-2	2.2e3
TPFA	1481	1386 + 95	1.1e-2	4.4e-3	2.7e-3	4.8e4
MPFA	1439	1348 + 91	1.1e-2	4.5e-3	8.0e-3	5.8e4
EDFM	1501	1369 + 132	6.5e-3	4.0e-3	3.3e-3	5.6e4
Flux-Mortar	3366	1280 + 75	1.0e-2	6.9e-3	1.8e-3	2.4e6
P-XFEM	1650	961 + 164	9.3e-2	7.3e-3	8.0e-3	9.3e9
D-XFEM	4474	1250 + 126	9.6e-3	8.9e-3	1.3e-3	1.2e6

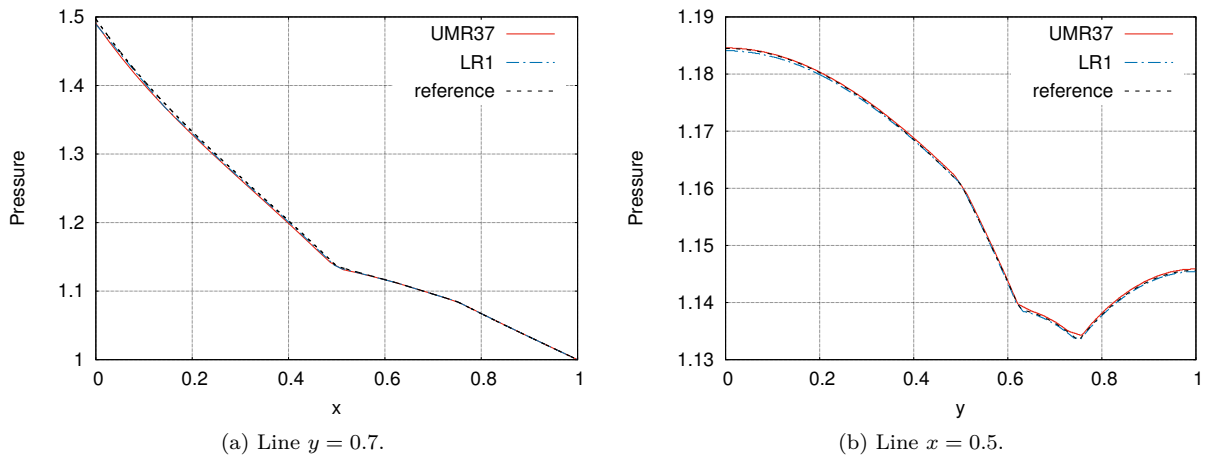


Figure 10: Benchmark 1 (pressure problem). Pressure solution along two lines.

Table 3: Benchmark 4 (pressure problem). DoF, number of elements, matrix density (nnz denotes number of non-zero entries in the system matrix) and matrix condition number for EFEM on different meshes compared to the corresponding methods in [19]. *No. of elements* for the methods in [19] are listed as matrix elements plus fracture elements.

Method	$N_{\text{dof}}$	No. of elements	$\text{nnz}/N_{\text{dof}}^2$	$\ \cdot\ _2\text{-cond}$
EFEM $\mathcal{M}_2^2$	5349	4623	1.3e-3	3.5e5
EFEM $\mathcal{M}_2^{2,r}$	9185	7629	7.2e-4	9.3e6
EFEM $\mathcal{M}_2^4$	33337	27666	2.0e-4	1.5e7*
EFEM $\mathcal{M}_2^{4,r}$	33924	28104	1.9e-4	6.4e7*
Box	5563	10807 + 1386	1.2e-3	9.3e5
TPFA	8481	7614 + 867	4.9e-4	5.3e6
MPFA	8588	7614 + 867	1.6e-3	4.9e6
EDFM	3599	2491 + 1108	1.4e-3	4.7e6
Flux-Mortar	25258	8319 + 1317	2.0e-4	2.2e17

\* Estimate of the 1-norm condition number based on MATLABs `cond` command.

Denote by  $\mathcal{M}_0$  the  $7 \times 6$  base mesh with  $h = 100$ . Then let  $\mathcal{M}_i^j$  be the mesh where  $\mathcal{M}_0$  is first refined globally  $i$  times, and then recursively refined locally around the fractures  $j$  times. With this  $h_{\min} = 100 \cdot 2^{-(i+j)}$  and  $h_{\max} = 100 \cdot 2^{-i}$ . Some of the fractures are very close without intersecting. It is important to resolve this geometrical aspect so that each vertex patch only see one fracture unless the fractures are connected. We denote by  $\mathcal{M}_i^{j,r}$  the mesh where  $\mathcal{M}_i^j$  is further locally refined to resolve close non-connected fractures. The DoFs and number of elements are reported in Table 3, along with the corresponding numbers for the methods considered in [19]. Fig. 12 displays two of the meshes and illustrates the effect of resolving the geometry.

Fig. 13 shows the pressure approximation on four different meshes. Observe that we have some instabilities in the solution in the upper right corner that vanish as we refine, see Fig. 14. This is due to the fact that one of the fractures cuts the corner and that we have zero Dirichlet condition at the right end of this fracture. Figs. 15 and 16 plots the pressure approximation along the lines  $y = 500$  and  $x = 625$ . Results on the highly refined mesh  $\mathcal{M}_6^6$ , where all geometry is sufficiently resolved, are included as a reference solution. We clearly see the effect of resolving the geometry, and we observe similar results to those reported in [19].

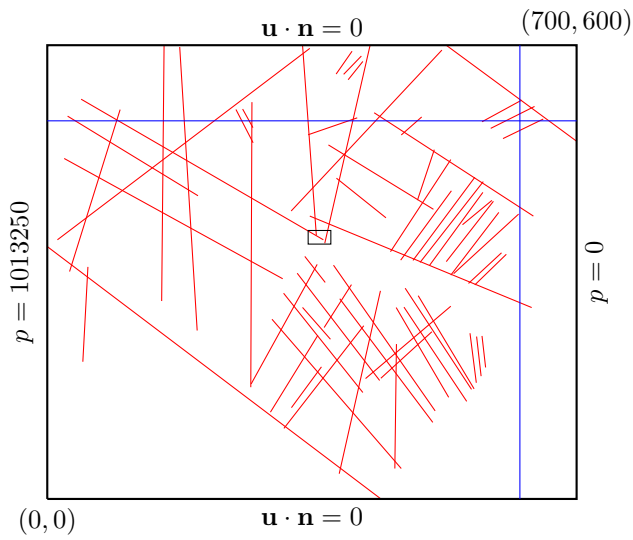


Figure 11: Benchmark 4 (pressure problem). Problem description with boundary conditions. The red lines represent fractures, the blue lines represent the lines for which the solution is plotted along in Figs. 15 and 16, and the small black box represents the box plotted in Fig. 12.

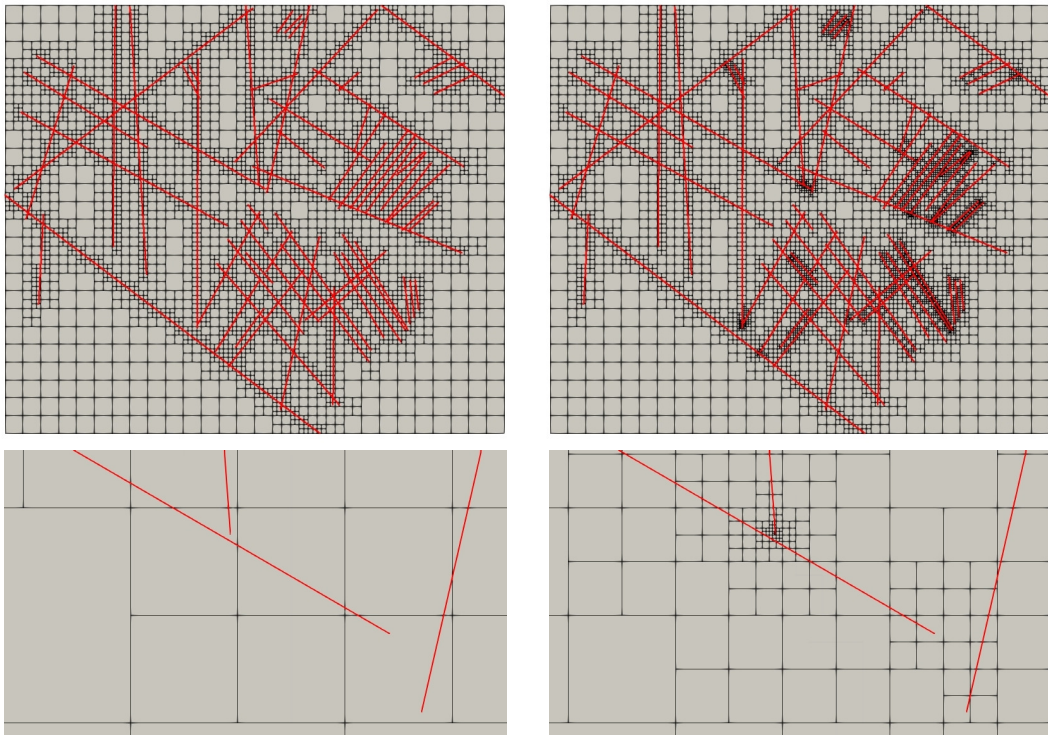


Figure 12: Benchmark 4 (pressure problem). Computational meshes,  $\mathcal{M}_2^2$  [left] and  $\mathcal{M}_2^{2,r}$  [right]. The top row displays the whole domain  $\Omega$ , while the bottom row displays the mesh on the small rectangle in the middle of Fig. 11.

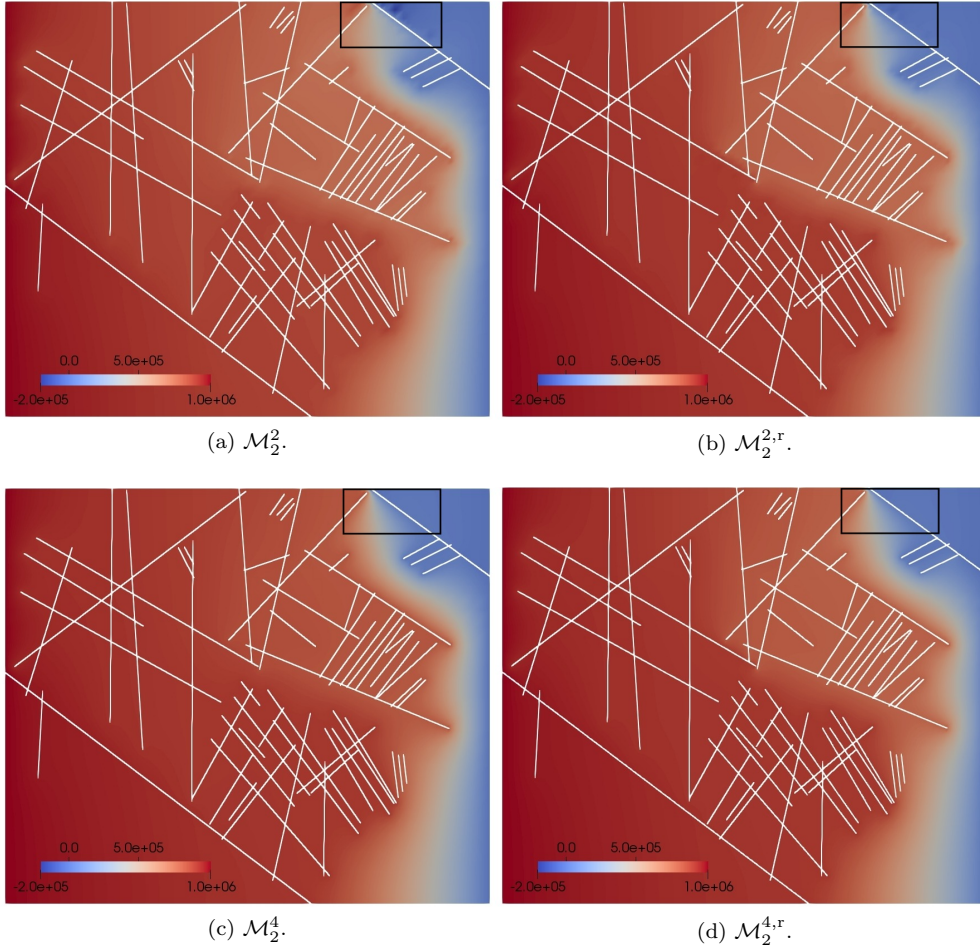


Figure 13: Benchmark 4 (pressure problem). Pressure approximation on different meshes. Zoom of the solution in the rectangular boxes are given in Fig. 14.

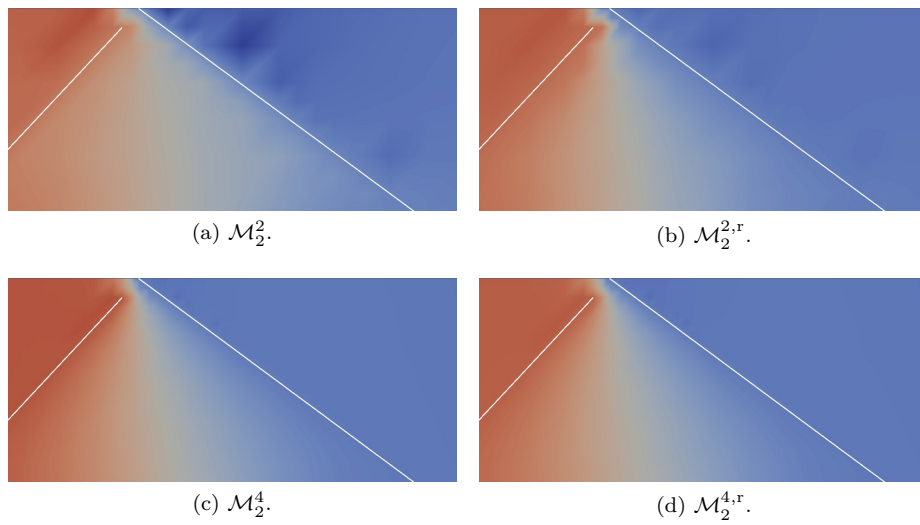


Figure 14: Benchmark 4 (pressure problem). Zoom of the pressure approximations depicted in Fig. 13 in the region represented by the rectangular boxes.

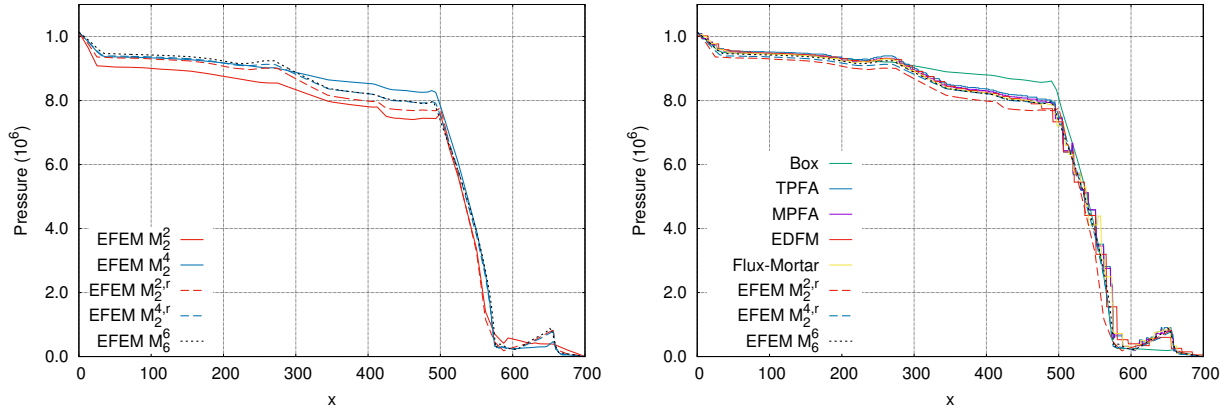


Figure 15: Benchmark 4. Pressure solution along the line  $y = 500$ . The solution on  $\mathcal{M}_6^6$  is considered as a reference solution.

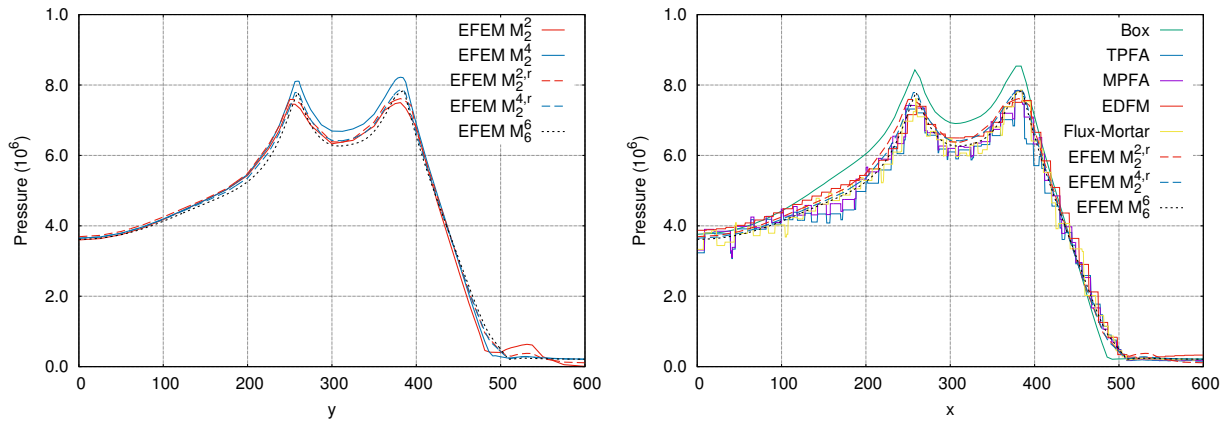


Figure 16: Benchmark 4 (pressure problem). Pressure solution along the line  $x = 625$ . The solution on  $\mathcal{M}_6^6$  is considered as a reference solution.

### 4.3. Coupled problems

We now couple the benchmark cases with the transport problem and solve for concentration. The coupled problem was not considered in [19].

#### 4.3.1. Benchmark 1: Regular fracture network

For the transport problem we set  $c_0 = 0$ , apply a boundary concentration  $c_B = 1$  on the inflow boundary ( $x = 0$ ), and let  $T = 0.5$ . We consider the same computational meshes as for the pressure problem. In addition, we construct a reference mesh with 182674 elements where the fractures are fully resolved, i.e.,  $h = w$  at the fractures and  $h \approx 16w$  away from the fractures. A reference solution is then obtained by a standard FV method on a continuous fracture model (no lower dimensional embedding), i.e., Eq. (3.29a) with  $\mathcal{K}_h^M = \mathcal{K}_h$  and  $\boldsymbol{\kappa} = \kappa_\Gamma \mathbf{I}$  in the elements in the fracture domain. Time steps for the reference solution is  $\Delta t = 1 \cdot 10^{-5}$ .

Fig. 17 shows the velocity approximations in each of the six fractures for the different meshes. We see a very good agreement, in particular for the LR meshes. This is as expected since the velocity is derived from the pressure solution, which was shown earlier to have higher accuracy when refining around the fractures.

For the transport problem, we define a quantity of interest, QOI, as the flux of concentration out of the two fractures on the right boundary face,

$$\text{QOI}_1(t) = (\mathbf{u}_\Gamma \cdot \mathbf{n}c)|_{\mathbf{x}=(1.0,0.5)}, \quad (4.7a)$$

$$\text{QOI}_2(t) = (\mathbf{u}_\Gamma \cdot \mathbf{n}c)|_{\mathbf{x}=(1.0,0.75)}. \quad (4.7b)$$

For the reference solution, these quantities are calculated as

$$\text{QOI}_1^{\text{ref}}(t) = \int_{0.5-\frac{w}{2}}^{0.5+\frac{w}{2}} (\mathbf{u} \cdot \mathbf{n}c)|_{x=1} dy, \quad (4.8a)$$

$$\text{QOI}_2^{\text{ref}}(t) = \int_{0.75-\frac{w}{2}}^{0.75+\frac{w}{2}} (\mathbf{u} \cdot \mathbf{n}c)|_{x=1} dy. \quad (4.8b)$$

First, we solve the coupled problem on the four uniform meshes with  $\Delta t = 1.0 \cdot 10^{-3}$ ,  $5.0 \cdot 10^{-4}$ ,  $2.5 \cdot 10^{-4}$ , and  $1.25 \cdot 10^{-4}$ , respectively, and on the three LR meshes with  $\Delta t = 5.0 \cdot 10^{-4}$ ,  $2.5 \cdot 10^{-4}$ , and  $1.25 \cdot 10^{-4}$ , respectively. The concentration solution on the finest meshes are displayed in Figs. 18 and 19, while QOI is plotted against time for all meshes in Fig. 20.

We observe similar solutions for all meshes. At early times and in fracture 1 ( $y = 0.5$ ), we have the best results on the LR meshes. However, the LR meshes are relatively coarse in the matrix. This causes large numerical diffusion and with time the concentration front in the matrix reaches the first vertical fracture ( $x = 0.5$ ). This explains why the solution on the LR meshes becomes inaccurate at large times. A better meshing for the coupled problem would be to refine both close to the fractures and in the left half of  $\Omega$ . Dynamic mesh adaptivity based on an a posteriori error estimator, see e.g. [43], could also improve the results, but this was not further examined in this work.

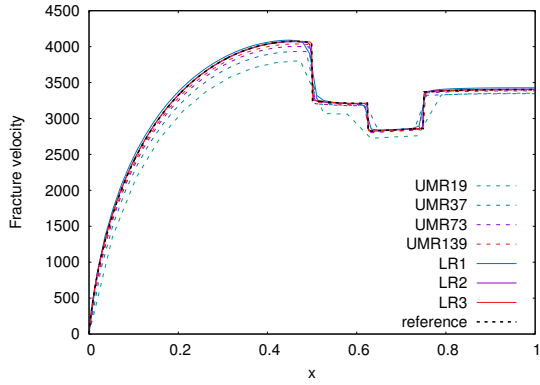
At last, we ran a series of simulations on the UMR meshes with  $\Delta t = 10^{-4}$  and compared to the reference solution by a  $L^2$  norm over the fractures, see Fig. 21. We get a higher convergence than what is expected from the lowest order FV method.

#### 4.3.2. Benchmark 4: A realistic case

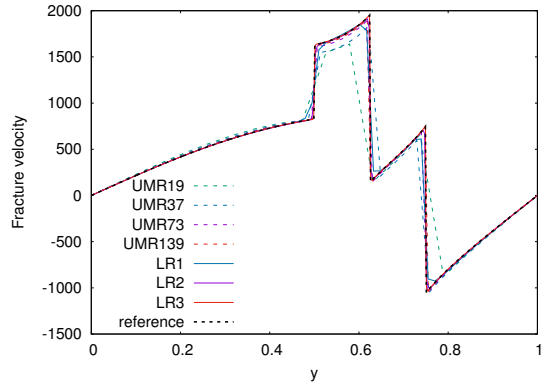
We now couple benchmark 4 to the transport problem, where  $c_0 = 0$  and an inflow concentration  $c_B = 1$  is set on the left boundary face. Such problem was also considered in [22], but with different permeabilities. We set the end time for the simulations to  $T = 100$  years<sup>3</sup>.

---

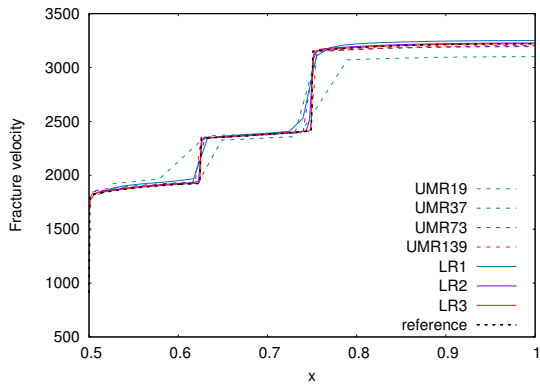
<sup>3</sup>1 year = 365 days.



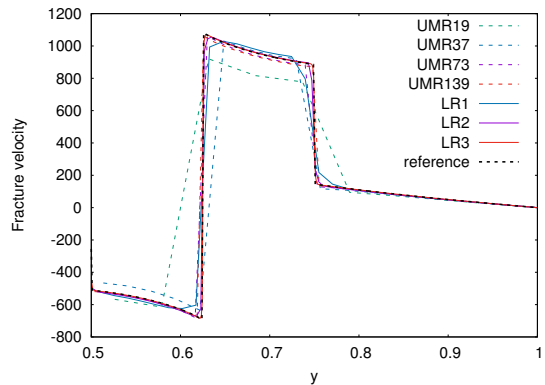
(a) Fracture 1 ( $y = 0.5$ )



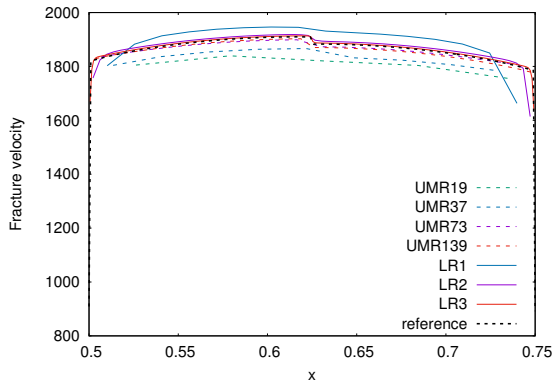
(b) Fracture 2 ( $x = 0.5$ )



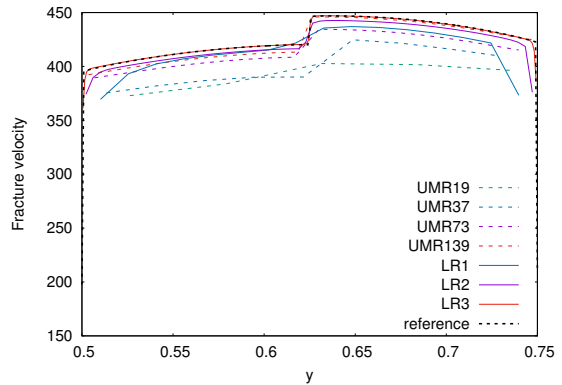
(c) Fracture 3 ( $y = 0.75$ )



(d) Fracture 4 ( $x = 0.75$ )



(e) Fracture 5 ( $y = 0.625$ )



(f) Fracture 6 ( $x = 0.625$ )

Figure 17: Benchmark 1 (coupled problem): Fracture velocities for the different meshes.

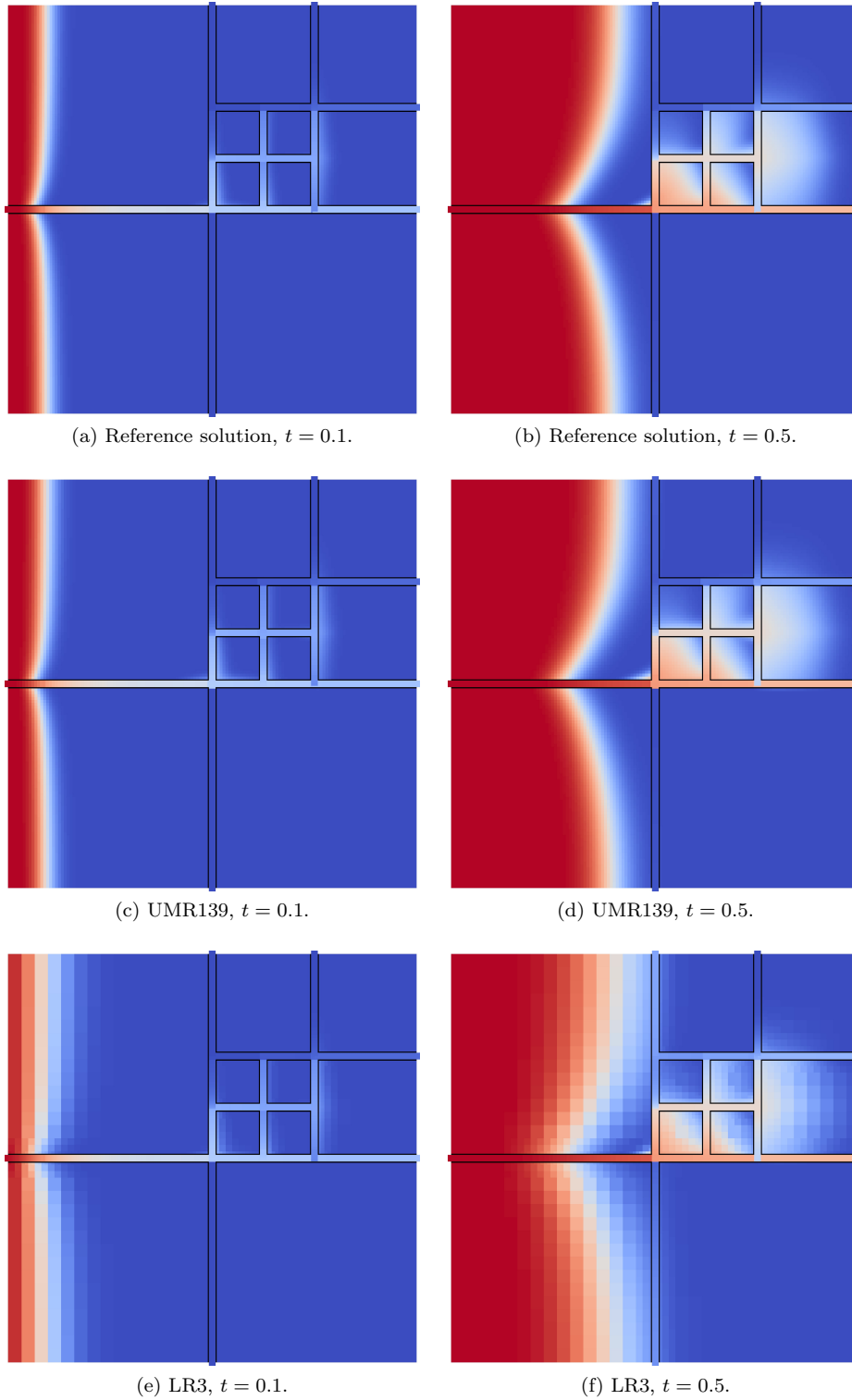


Figure 18: Benchmark 1 (coupled problem). Concentration solution. The fractures are visualized with a fixed exaggerated width. Number of degrees of freedom,  $N_{\text{dof}}$ , is 182674 for the reference solution (continuum model), 19321 for UMR139, and 16252 for LR3.

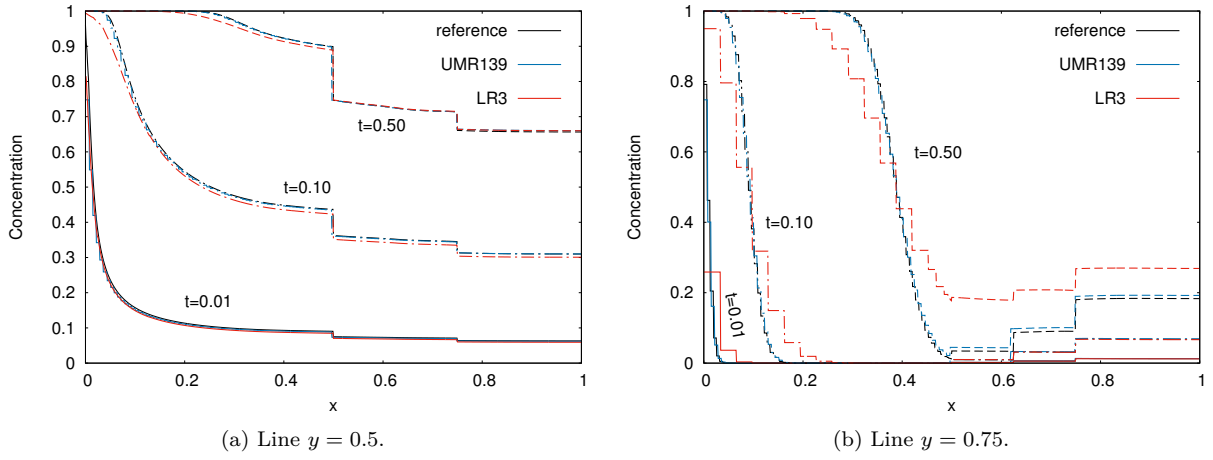


Figure 19: Benchmark 1 (coupled problem). Concentration solution along two lines at different times.

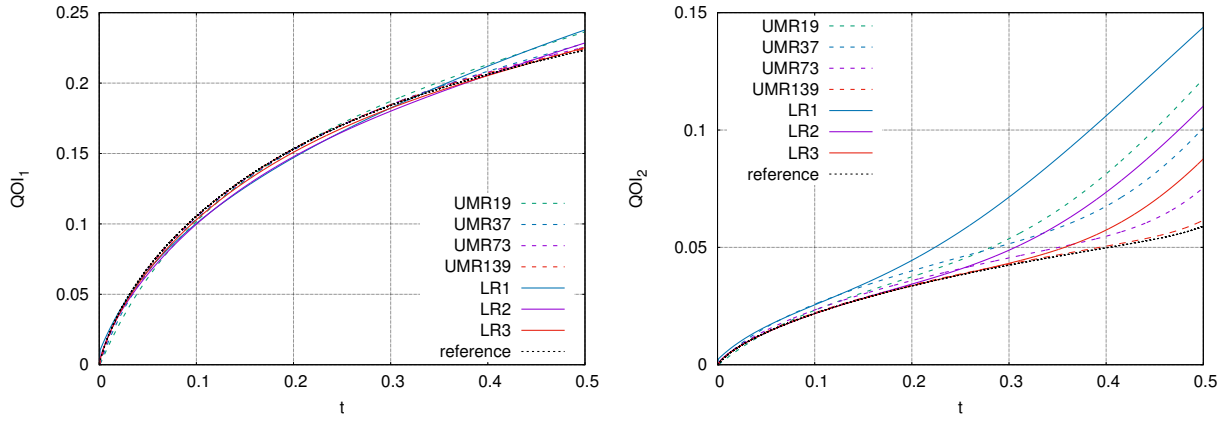


Figure 20: Benchmark 1 (coupled problem). Quantity of interest,  $QOI_i$ ,  $i = 1, 2$ , as functions of time.

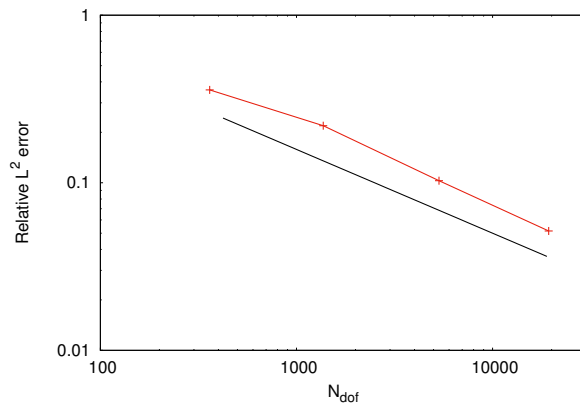


Figure 21: Benchmark 1 (coupled problem). Relative concentration error in fractures,  $\frac{\|c_{\text{ref}} - c_h\|_{L^2(\Gamma)}}{\|c_{\text{ref}}\|_{L^2(\Gamma)}}$ , at  $t = T$  against  $N_{\text{dof}}$ . The reference solution is compared against the solution on the UMR meshes with  $\Delta t = 1 \cdot 10^{-4}$ . The black reference line has slope  $-0.5$ .

First, we set  $\Delta t = 1$  hour (36500 time steps), and consider the meshes  $\mathcal{M}_2^{j,r}$ . Concentration solutions in the fractures are displayed in Fig. 22. Furthermore, convergence of the concentration in the fractures is demonstrated in Fig. 23. Due to the high fracture permeability, nearly all transport take place in the fractures, and hence we do not display the matrix solution. We observe that we get reasonable good results even for the coarsest mesh. Furthermore, the results for  $\mathcal{M}_2^4$  clearly illustrates the importance of resolving the geometry, as the solution is far off in some of the fractures, even compared to  $\mathcal{M}_2^{2,r}$  which has much less DoFs. Convergence is rather slow due to the low order method.

Next, we ran a series of simulations on  $\mathcal{M}_2^{2,r}$  with  $\Delta t = \{20, 50, 100, 365\}$  days and compared to the solution with  $\Delta t = 1$  hour on the same mesh. The  $L^2$  error over  $\Omega$  at  $t = T$  is plotted against  $(\Delta t)^{-1}$  in Fig. 24, and we observe linear convergence in time as expected.

## 5. Concluding remarks

This article addresses the *numerical solution of a coupled flow and transport problem* in fractured porous media, where the *fractures are modeled as lower-dimensional interfaces* embedded in the surrounding matrix. The proposed solution strategy includes three main steps: (1) Solving the flow problem with an embedded finite element method (EFEM) [11]; (2) Locally conservative flux approximation; and (3) Solving the transport problem with a non-standard lowest order finite volume (FV) method.

*The main contribution of this work is that we couple EFEM with a numerical model for the transport problem.* EFEM allows for complex fracture geometry, where the fractures can cut the elements arbitrarily, and compared to other embedded discrete fracture-matrix models, there are no lower-dimensional elements along the fractures. The numerical model for the transport problem presented in this work, aims to be as flexible as EFEM with respect to meshing. This is resolved by a lowest order upwind FV method where the fracture solution is represented by elements cut by the fracture. The main novelty in our method is how we approximate the coupling term between the matrix and the fractures.

Furthermore, this work includes the following contributions:

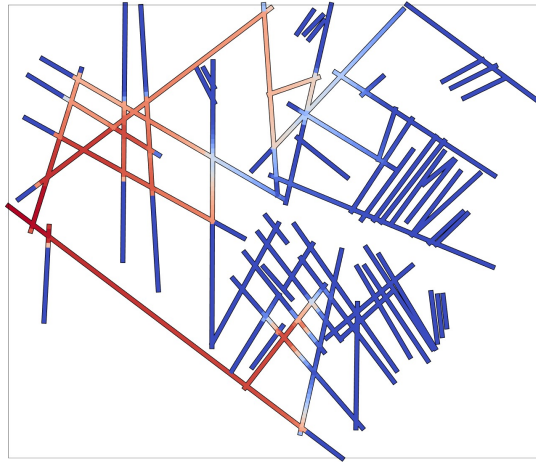
- We apply EFEM to realistic benchmark problems presented in [19]. Our results are in good agreement with the results in [19] and in some cases EFEM is most accurate. Applying a priori local refinement based on an estimate in [11] gives especially good results.
- To ensure locally conservative fluxes, we adapt and apply the postprocessing method presented in [37].
- We demonstrate the abilities of our coupled solution strategy by numerical examples on a realistic case with a complex fracture network.

*A main advantage of our method compared to other discrete fracture-matrix models, is the inherent simplicity*, both in terms of formulation, implementation and meshing. Despite the simplicity, the presented results are promising.

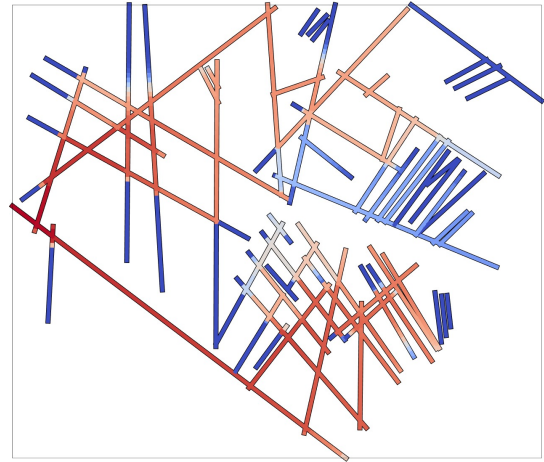
One direction for further work is to consider adaptive routines for the transport solver, perhaps looking at the space-time approach allowing for easy handling of local time refinement. Rigorous convergence proofs and error estimates for the transport solver are also desired. Moreover, one could pursue including more physics into the model, e.g., multi-phase flow. To reduce the numerical diffusion associated with the implicit Euler method, one could consider higher order time integration, e.g., [33].

## Acknowledgements

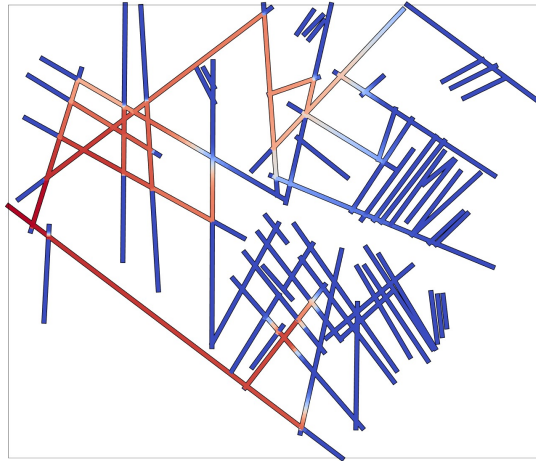
LHO is funded by VISTA (Grant No. 6355) — a basic research program funded by Statoil, conducted in close collaboration with The Norwegian Academy of Science and Letters. MGL was supported by The Swedish Foundation for Strategic Research Grant No. AM13-0029, and the Swedish Research Council Grants Nos. 2013-4708, 2017-03911. The authors appreciate the open access to the results given in the benchmark paper [19]. Furthermore, the authors thank Karl Larsson, Department of Mathematics and Mathematical Statistics, Umeå University, for his help with visualization of the results in Figs. 18 and 22.



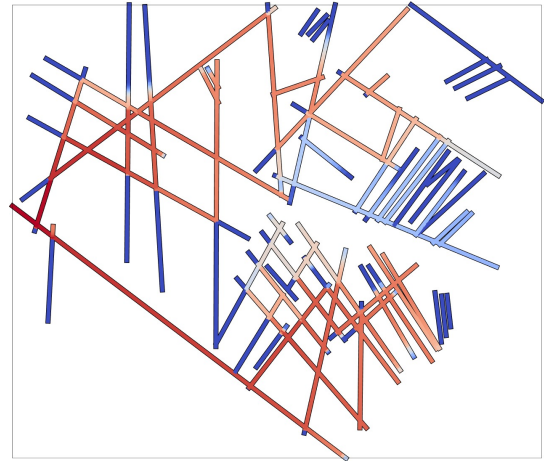
(a)  $\mathcal{M}_2^{2,r}$ ,  $t = 15$  years.



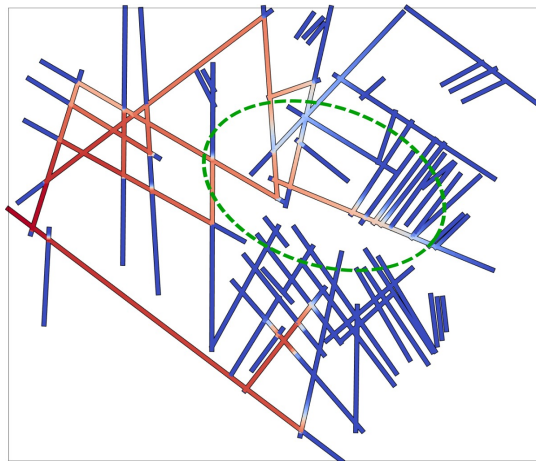
(b)  $\mathcal{M}_2^{2,r}$ ,  $t = 100$  years.



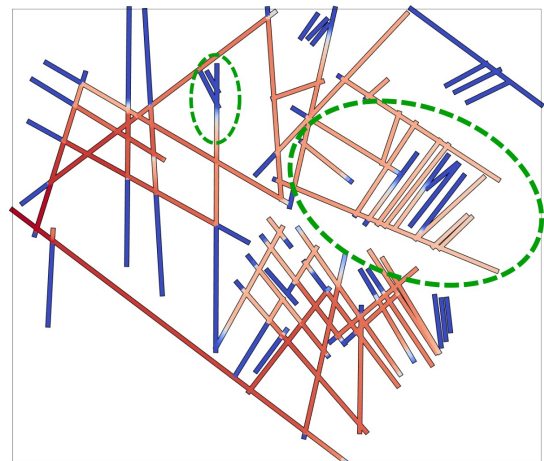
(c)  $\mathcal{M}_2^{4,r}$ ,  $t = 15$  years.



(d)  $\mathcal{M}_2^{4,r}$ ,  $t = 100$  years.



(e)  $\mathcal{M}_2^4$ ,  $t = 15$  years.



(f)  $\mathcal{M}_2^4$ ,  $t = 100$  years.

Figure 22: Benchmark 4 (coupled problem). Concentration solutions in fractures. The fractures are displayed with a fixed (exaggerated) width. Regions where the results on the non-resolved mesh  $\mathcal{M}_2^4$  deviates substantially from the other two meshes are marked with green dashed ellipses.

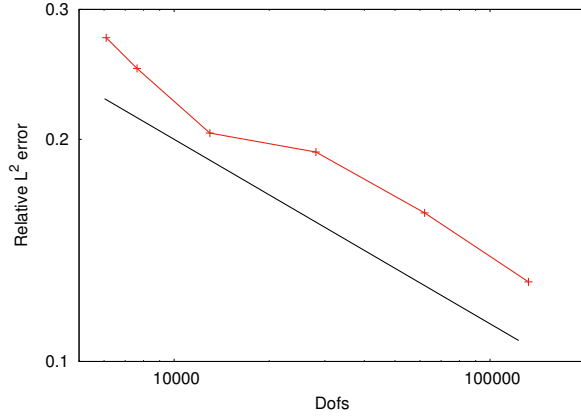


Figure 23: Benchmark 4 (coupled problem). Relative concentration error in fractures,  $\frac{\|c_{\text{ref}} - c_h\|_{L^2(\Gamma)}}{\|c_{\text{ref}}\|_{L^2(\Gamma)}}$ , at  $t = T$  against  $N_{\text{dof}}$ . The solution on  $\mathcal{M}_2^{8,r}$  is used as reference solution,  $c_{\text{ref}}$ , and compared against the solutions on  $\mathcal{M}_2^{j,r}$  for  $j = 1, 2, \dots, 6$ . All simulations are run with  $\Delta t = 1$  day. The black reference line has slope  $-0.25$ .

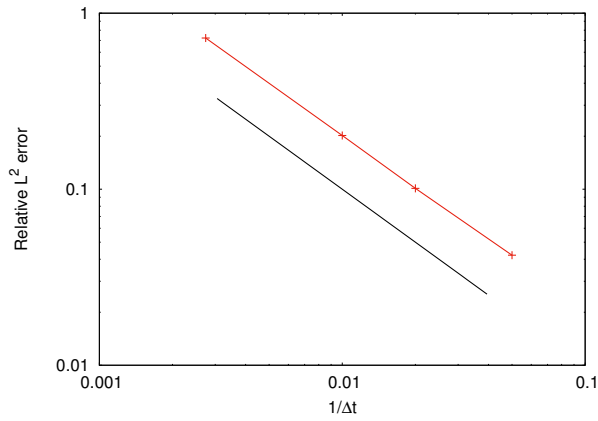


Figure 24: Benchmark 4 (coupled problem). Relative concentration error,  $\frac{\|c_{\text{ref}} - c_h\|_{L^2(\Omega)}}{\|c_{\text{ref}}\|_{L^2(\Omega)}}$ , at  $t = T$  against  $1/\Delta t$ . All simulations are run on  $\mathcal{M}_2^{2,r}$ . The solution with  $\Delta t = 1$  hour is used as reference solution,  $c_{\text{ref}}$ , and compared to the solutions with  $\Delta t = \{20, 50, 100, 365\}$  days. The black reference line has slope  $-1$ .

## Appendix

### A.1. Discontinuous Galerkin formulation

We formulate here a lowest order Discontinuous Galerkin method (DG(0)) with upwinding for the transport problem, Eq. (2.14). This formulation is equivalent to the finite volume method derived in Section 3.3. We include it here for convenience of the reader more familiar with DG methods. The DG formulation is also more suitable for deriving error estimates.

We start by multiplying Eq. (2.14a) by a test function  $v$ , integrate over an element  $K \in \mathcal{K}_h^M$  and apply Greens formula to obtain

$$\int_K \phi \frac{\partial c}{\partial t} v - \int_K \mathbf{c} \mathbf{u} \cdot \nabla v + \int_{\partial K} \mathbf{u} \cdot \mathbf{n}_K c v = \int_K f(c) v, \quad K \in \mathcal{K}_h^M. \quad (\text{A.1})$$

Summing the boundary term over all  $K \in \mathcal{K}_h^M$  we get

$$\begin{aligned} \sum_{K \in \mathcal{K}_h^M} \int_{\partial K} \mathbf{u} \cdot \mathbf{n}_K c v = & - \sum_{F \in \mathcal{F}_{h,1}^M} \int_F \mathbf{u} \cdot \mathbf{n}_F c \llbracket v \rrbracket + \sum_{F \in \mathcal{F}_{h,1}^{\text{FM}}} \int_F \mathbf{u} \cdot \mathbf{n}_{\text{MF}} c v \\ & + \sum_{F \in \mathcal{F}_{h,\text{out}}^M} \int_F \mathbf{u} \cdot \mathbf{n}_F c v + \sum_{F \in \mathcal{F}_{h,\text{in}}^M} \int_F \mathbf{u} \cdot \mathbf{n}_F c_B v. \end{aligned} \quad (\text{A.2})$$

We have denoted by  $\mathbf{n}_{\text{MF}}$  the unit normal on  $F \in \mathcal{F}_{h,1}^{\text{FM}}$  pointing from the matrix domain towards the fracture.

Similarly, we multiply Eq. (2.14b) by a test function  $v_\Gamma$ , integrate over  $K \cap \Gamma$ , for  $K \in \mathcal{K}_h^F$ , and apply Greens formula to obtain

$$\int_{K \cap \Gamma} w \phi_\Gamma \frac{\partial c_\Gamma}{\partial t} v_\Gamma - \int_{K \cap \Gamma} c_\Gamma \mathbf{u}_\Gamma \cdot \nabla_\Gamma v_\Gamma + \int_{\partial(K \cap \Gamma)} \mathbf{u}_\Gamma \cdot \mathbf{n}_{K \cap \Gamma} c_\Gamma v_\Gamma - \int_{K \cap \Gamma} \llbracket \mathbf{u} \cdot \mathbf{n} c^* \rrbracket v_\Gamma = \int_{K \cap \Gamma} f_\Gamma(c_\Gamma) v_\Gamma. \quad (\text{A.3})$$

Again, summing the boundary term over all  $K \in \mathcal{K}_h^F$  we get

$$\begin{aligned} \sum_{K \in \mathcal{K}_h^F} \int_{\partial(K \cap \Gamma)} \mathbf{u}_\Gamma \cdot \mathbf{n}_{K \cap \Gamma} c_\Gamma v_\Gamma = & - \sum_{F \in \mathcal{F}_{h,1}^F} (\mathbf{u}_\Gamma \cdot \mathbf{t}_{\Gamma,F} c_\Gamma \llbracket v_\Gamma \rrbracket) |_{F \cap \Gamma} \\ & + \sum_{F \in \mathcal{F}_{h,\text{in}}^F} (\mathbf{u}_\Gamma \cdot \mathbf{t}_{\Gamma,F} c_{\Gamma,B} v_\Gamma) |_{F \cap \Gamma} + \sum_{F \in \mathcal{F}_{h,\text{out}}^F} (\mathbf{u}_\Gamma \cdot \mathbf{t}_{\Gamma,F} c_\Gamma v_\Gamma) |_{F \cap \Gamma}, \end{aligned} \quad (\text{A.4})$$

where  $\mathbf{t}_{\Gamma,F}$  is the unit tangent to  $\Gamma$  oriented in the same direction as  $\mathbf{n}_F$ .

To formulate the DG method, we replace  $c$  and  $c_\Gamma$  by  $c_h \in Q_0(\mathcal{K}_h)$  and  $\varphi$  and  $\varphi_\Gamma$  by  $\varphi_h \in Q_0(\mathcal{K}_h)$ . Furthermore, we approximate the coupling term as follows,

$$\int_{K \cap \Gamma} \llbracket \mathbf{u} \cdot \mathbf{n} c_h^* \rrbracket v_h \approx \sum_{\tilde{K} \in \mathcal{K}_h^M} \int_{\partial \tilde{K} \cap \partial K} (\mathbf{n}_F \cdot \mathbf{n}_K) \mathbf{u} \cdot \mathbf{n}_F c_h v_h. \quad (\text{A.5})$$

This is equivalent to the approximation (3.16). Summing this term over all  $K \in \mathcal{K}_h^F$  we get

$$\sum_{K \in \mathcal{K}_h^F} \int_{K \cap \Gamma} \llbracket \mathbf{u} \cdot \mathbf{n} c_h^* \rrbracket v_h \approx \sum_{F \in \mathcal{F}_{h,1}^{\text{FM}}} \int_F \mathbf{u} \cdot \mathbf{n}_{\text{MF}} c_h v_h. \quad (\text{A.6})$$

Adding everything up, we end up the following formulation. Find  $c_h \in Q_0(\mathcal{K}_h)$  such that

$$b(c_h, v_h) = k(v_h), \quad \forall v_h \in Q_0(\mathcal{K}_h), \quad (\text{A.7})$$

where

$$\begin{aligned}
b(c, v) &= \sum_{K \in \mathcal{K}_h^M} \int_K \left( \phi \frac{\partial c}{\partial t} cv + \check{q} cv \right) + \sum_{K \in \mathcal{K}_h^F} \int_{K \cap \Gamma} \left( w \phi_\Gamma \frac{\partial c}{\partial t} v + \check{q}_\Gamma cv \right) \\
&\quad - \sum_{F \in (\mathcal{F}_{h,i} \setminus \mathcal{F}_{h,i}^F)} \int_F \mathbf{u} \cdot \mathbf{n}_F c[v] - \sum_{F \in \mathcal{F}_{h,i}^F} (\mathbf{u}_\Gamma \cdot \mathbf{t}_{\Gamma,F} c[v])|_{F \cap \Gamma} \\
&\quad + \sum_{F \in \mathcal{F}_{h,out}^M} \int_F \mathbf{u} \cdot \mathbf{n}_F cv + \sum_{F \in \mathcal{F}_{h,out}^F} (\mathbf{u}_\Gamma \cdot \mathbf{t}_{\Gamma,F} cv)|_{F \cap \Gamma}
\end{aligned} \tag{A.8}$$

and

$$k(v) = \sum_{K \in \mathcal{K}_h^M} \int_K \hat{q} c_w v + \sum_{K \in \mathcal{K}_h^F} \int_{K \cap \Gamma} \hat{q}_\Gamma c_w v + \sum_{F \in \mathcal{F}_{h,in}^M} \int_F \mathbf{u} \cdot \mathbf{n}_F c_B v + \sum_{F \in \mathcal{F}_{h,in}^F} (\mathbf{u}_\Gamma \cdot \mathbf{t}_{\Gamma,F} c_{\Gamma,B} v)|_{F \cap \Gamma}. \tag{A.9}$$

We have used the definition of  $f(c)$  and  $f_\Gamma(c_\Gamma)$ , see Eq. (2.15). For the concentration on faces  $F \in \mathcal{F}_h$ , we use the upwind approximation

$$\mathbf{u} \cdot \mathbf{n}_F c_h = \begin{cases} \mathbf{u} \cdot \mathbf{n}_F (c_h)_-, & \text{if } \mathbf{u} \cdot \mathbf{n}_F \geq 0, \\ \mathbf{u} \cdot \mathbf{n}_F (c_h)_+, & \text{if } \mathbf{u} \cdot \mathbf{n}_F < 0. \end{cases} \tag{A.10}$$

Applying the velocity model described by Eqs. (3.18)–(3.27), we may simplify the forms  $b(\cdot, \cdot)$  and  $k(\cdot)$  for the coupled problem by a similar approach as described by Eq. (3.19), so that

$$b(c, v) = \sum_{K \in \mathcal{K}_h^M} \int_K \left( \phi \frac{\partial c}{\partial t} cv + \check{q} cv \right) + \sum_{K \in \mathcal{K}_h^F} \int_{K \cap \Gamma} \left( w \phi_\Gamma \frac{\partial c}{\partial t} v + \check{q}_\Gamma cv \right) - \sum_{F \in \mathcal{F}_{h,i}} \int_F V_h c[v] + \sum_{F \in \mathcal{F}_{h,out}} \int_F V_h cv \tag{A.11}$$

and

$$k(v) = \sum_{K \in \mathcal{K}_h^M} \int_K \hat{q} c_w v + \sum_{K \in \mathcal{K}_h^F} \int_{K \cap \Gamma} \hat{q}_\Gamma c_w v + \sum_{F \in \mathcal{F}_{h,in}^M} \int_F V_h c_B v + \sum_{F \in \mathcal{F}_{h,in}^F} \int_F V_h c_{\Gamma,B} v. \tag{A.12}$$

If we apply implicit Euler as time integrator, we end up with a scheme that is equivalent to the FV-IE scheme in Eq. (3.29).

### A.2. Interpretation of concentration solution

The numerical method given by Eq. (3.29) defines a constant solution on  $K \in \mathcal{K}_h^F$ . However,  $K$  originally contains both a fractured domain represented as a lower-dimensional interface,  $K \cap \Gamma$ , and a matrix domain  $K \setminus \Gamma$ . Let  $\{K_j\}_{j \in \{1, \dots, N_K\}}$  be a partition of  $K$  into  $N_K$  subelements defined by  $\Gamma$ . For a single fracture cutting  $K$ , we have  $n_K = 2$ , but for intersecting and bifurcating fractures in  $K$ ,  $n_K$  can be larger. For a terminating fracture, we have  $n_K = 1$ . We interpret the solution on  $K$  by assigning a constant value to each subelement  $K_j$  and one value on the fracture intersection  $K \cap \Gamma$ . Let  $\hat{c}_h$  denote the interpreted solution. Then we define

$$\hat{c}_h|_K = c_h|_K, \quad \forall K \in \mathcal{K}_h^M, \tag{A.13}$$

$$\hat{c}_h|_{K \cap \Gamma} = c_h|_K, \quad \forall K \in \mathcal{K}_h^F. \tag{A.14}$$

It is not as easy to define the interpreted solution on the fracture subelements, but the following algorithm can be used. Denote by  $\mathcal{K}_h^{M,i}$  the (non-empty) subsets of  $\mathcal{K}_h^M$  with elements contained in  $\Omega_i$ , i.e.,

$$\mathcal{K}_h^{M,i} = \{K \in \mathcal{K}_h^M : K \subset \Omega_i\}. \tag{A.15}$$

Furthermore, let  $\mathcal{K}_h^{F,i}$  be the set of all fracture subelements contained in  $\Omega_i$ , i.e.,

$$\mathcal{K}_h^{F,i} = \{K_j \in \mathcal{K} : K_j \subset \Omega_i, K_j \in \mathcal{K}_h^F\}. \quad (\text{A.16})$$

At last, denote by  $\mathcal{N}_K(F)$  the neighbor of  $K$  that shares face  $F$ .

Algorithm 1 recursively assigns values to each element  $\tilde{K} \in \mathcal{K}_h^{F,i}$ . Once a value is assigned to  $\tilde{K}$ , we move  $\tilde{K}$  from  $\mathcal{K}_h^{F,i}$  to  $\mathcal{K}_h^{M,i}$ . In this way we mark  $\tilde{K}$  as assigned and also allow for its value to be further assigned to another neighbor in the next cycle. The algorithm works under the mild assumption that there is at least one matrix element for each subdomain, i.e., for all  $\Omega_i$ ,  $i = 1, 2, \dots, n_d$ , there is an  $K \in \mathcal{K}_h^M$  such that  $K \subset \Omega_i$ . Moreover, we remark that the algorithm is sensitive to the ordering of elements. We refer to Fig. 3 for an illustrative example of how this algorithm works. Finally, we emphasize that this algorithm is purely for the interpretation of the results, and not part of the numerical method.

---

**Algorithm 1:** Assigning values to fracture subelements

---

```

for  $i = 1, \dots, n_d$  do
  while  $\mathcal{K}_h^{M,i} \neq \emptyset$  do
    for  $K \in \mathcal{K}_h^{M,i}$  do
      for  $F \in \partial K$  do
         $\tilde{K} = \mathcal{N}_K(F)$ 
        if  $\tilde{K} \in \mathcal{K}_h^{F,i}$  then
           $\hat{c}_h|_{\tilde{K}} = c_h|_K$ 
           $\mathcal{K}_h^{F,i} = \mathcal{K}_h^{F,i} \setminus \{\tilde{K}\}$ 
           $\mathcal{K}_h^{M,i} = \mathcal{K}_h^{M,i} \cup \{\tilde{K}\}$ 
        end
      end
    end
  end
end

```

---

## References

- [1] ALBOIN, C., JAFFRÉ, J., ROBERTS, J. E., AND SERRES, C. Modeling fractures as interfaces for flow and transport in porous media. In *Fluid Flow and Transport in Porous Media: Mathematical and Numerical Treatment* (2002), Z. Chen and R. E. Ewing, Eds., vol. 295 of *Contemporary Mathematics*, AMS, pp. 13–24.
- [2] ALBOIN, C., JAFFRÉ, J., ROBERTS, J. E., WANG, X., AND SERRES, C. Domain decomposition for some transmission problems in flow in porous media. In *Numerical Treatment of Multiphase Flows in Porous Media*. Springer, 2000, pp. 22–34.
- [3] ANGOT, P. A model of fracture for elliptic problems with flux and solution jumps. *Comptes Rendus Mathématique* 337, 6 (2003), 425–430.
- [4] ANGOT, P., BOYER, F., AND HUBERT, F. Asymptotic and numerical modelling of flows in fractured porous media. *ESAIM: Mathematical Modelling and Numerical Analysis* 43, 2 (2009), 239–275.
- [5] ANTONIETTI, P. F., FACCIOLA, C., RUSSO, A., AND VARANI, M. Discontinuous Galerkin approximation of flows in fractured porous media on polytopic grids. Tech. Rep. 55, MOX, Politecnico di Milano, 2016.
- [6] ANTONIETTI, P. F., FORMAGGIA, L., SCOTTI, A., VERANI, M., AND VERZOTT, N. Mimetic finite difference approximation of flows in fractured porous media. *ESAIM: Mathematical Modelling and Numerical Analysis* 50, 3 (2016), 809–832.
- [7] BANGERTH, W., HARTMANN, R., AND KANSCHAT, G. deal.II—a general-purpose object-oriented finite element library. *ACM Trans. Math. Softw.* 33, 4 (2007).
- [8] BOON, W. M., NORDBOTTEN, J. M., AND YOTOV, I. Robust discretization of flow in fractured porous media. arXiv:1601.06977 [math.NA], 2016.
- [9] BRENNER, K., HENNICKER, J., MASSON, R., AND SAMIER, P. Gradient discretization of hybrid-dimensional Darcy flow in fractured porous media with discontinuous pressures at matrix–fracture interfaces. *IMA Journal of Numerical Analysis* 37, 3 (2016), 1551–1585.
- [10] BURMAN, E., CLAUS, S., HANSBO, P., LARSON, M. G., AND MASSING, A. Cutfem: Discretizing geometry and partial differential equations. *International Journal for Numerical Methods in Engineering* 104, 7 (2015), 472–501.

- [11] BURMAN, E., HANSBO, P., AND LARSON, M. G. A simple finite element method for elliptic bulk problems with embedded surfaces. arXiv:1709.00972 [math.NA], 2017.
- [12] BURMAN, E., HANSBO, P., LARSON, M. G., AND LARSSON, K. Cut finite elements for convection in fractured domains. arXiv:1801.06103 [math.NA], 2018.
- [13] BURMAN, E., HANSBO, P., LARSON, M. G., AND SAMVIN, D. A cut finite element method for elliptic bulk problems with embedded surfaces. arXiv:1805.00693 [math.NA], 2018.
- [14] CAPATINA, D., LUCE, R., EL-OTMANY, H., AND BARRAU, N. Nitsche’s extended finite element method for a fracture model in porous media. *Applicable Analysis* 95, 10 (2016), 2224–2242.
- [15] D’ANGELO, C., AND SCOTTI, A. A mixed finite element method for Darcy flow in fractured porous media with non-matching grids. *ESAIM: Mathematical Modelling and Numerical Analysis* 46, 2 (2012), 465–489.
- [16] DE ARAUJO CAVALCANTE FILHO, J. S., SHAKIBA, M., MOINFAR, A., AND SEPEHRNOORI, K. Implementation of a preprocessor for embedded discrete fracture modeling in an IMPEC compositional reservoir simulator. In *SPE Reservoir Simulation Symposium* (2015), Society of Petroleum Engineers.
- [17] FAILLE, I., FLAURAUD, E., NATAF, F., PÉGAZ-FIORNET, S., SCHNEIDER, F., AND WILLIEN, F. A new fault model in geological basin modelling. Application of finite volume scheme and domain decomposition methods. In *Finite volumes for complex applications* (2002), vol. 3, pp. 543–550.
- [18] FAILLE, I., FUMAGALLI, A., JAFFRÉ, J., AND ROBERTS, J. E. Model reduction and discretization using hybrid finite volumes for flow in porous media containing faults. *Computational Geosciences* 20, 2 (2016), 317–339.
- [19] FLEMISCH, B., BERRE, I., BOON, W., FUMAGALLI, A., SCHWENCK, N., SCOTTI, A., STEFANSSON, I., AND TATOMIR, A. Benchmarks for single-phase flow in fractured porous media. *Advances in Water Resources* 111 (2018), 239–258.
- [20] FORMAGGIA, L., FUMAGALLI, A., SCOTTI, A., AND RUFFO, P. A reduced model for Darcy’s problem in networks of fractures. *ESAIM: Mathematical Modelling and Numerical Analysis* 48, 4 (2014), 1089–1116.
- [21] FRIH, N., MARTIN, V., ROBERTS, J. E., AND SAÂDA, A. Modeling fractures as interfaces with nonmatching grids. *Computational Geosciences* 16, 4 (2012), 1043–1060.
- [22] FUMAGALLI, A., AND KEILEGAVLEN, E. Dual virtual element methods for discrete fracture matrix models. arXiv:1711.01818 [math.NA], 2017.
- [23] FUMAGALLI, A., AND SCOTTI, A. A reduced model for flow and transport in fractured porous media with non-matching grids. In *Numerical Mathematics and Advanced Applications 2011*. Springer, 2013, pp. 499–507.
- [24] GEIGER, S., ROBERTS, S., MATTHÄI, S., ZOPPOU, C., AND BURRI, A. Combining finite element and finite volume methods for efficient multiphase flow simulations in highly heterogeneous and structurally complex geologic media. *Geofluids* 4, 4 (2004), 284–299.
- [25] HAJIBEYGI, H., KARVOUNIS, D., AND JENNY, P. A hierarchical fracture model for the iterative multiscale finite volume method. *Journal of Computational Physics* 230, 24 (2011), 8729–8743.
- [26] HUANG, H., LONG, T. A., WAN, J., AND BROWN, W. P. On the use of enriched finite element method to model subsurface features in porous media flow problems. *Computational Geosciences* 15, 4 (2011), 721–736.
- [27] JIANG, J., AND YOUNIS, R. M. An improved projection-based embedded discrete fracture model (pEDFM) for multiphase flow in fractured reservoirs. *Advances in Water Resources* 109 (2017), 267–289.
- [28] KARIM-FARD, M., AND FIROOZABADI, A. Numerical simulations of water injection in fractured media using the discrete-fracture model and the galerkin method. *SPE Reservoir Evaluation & Engineering* 6, 02 (2003), 117–126.
- [29] KARIMI-FARD, M., AND DURLOFSKY, L. J. A general gridding, discretization, and coarsening methodology for modeling flow in porous formations with discrete geological features. *Advances in Water Resources* 96 (2016), 354–372.
- [30] LARSON, M. G., AND NIKLASSON, A. J. A conservative flux for the continuous Galerkin method based on discontinuous enrichment. *Calcolo* 41, 2 (2004), 65–76.
- [31] LI, L., AND LEE, S. H. Efficient field-scale simulation of black oil in a naturally fractured reservoir through discrete fracture networks and homogenized media. *SPE Reservoir Evaluation & Engineering* 11, 04 (2008), 750–758.
- [32] MARTIN, V., JAFFRÉ, J., AND ROBERTS, J. E. Modeling fractures and barriers as interfaces for flow in porous media. *SIAM Journal on Scientific Computing* 26, 5 (2005), 1667–1691.
- [33] MATTHÄI, S. K., NICK, H. M., PAIN, C., AND NEUWEILER, I. Simulation of solute transport through fractured rock: a higher-order accurate finite-element finite-volume method permitting large time steps. *Transport in porous media* 83, 2 (2010), 289–318.
- [34] MOINFAR, A., VARAVEI, A., SEPEHRNOORI, K., AND JOHNS, R. T. Development of an efficient embedded discrete fracture model for 3D compositional reservoir simulation in fractured reservoirs. *SPE Journal* 10, 02 (2014).
- [35] MORALES, F., AND SHOWALTER, R. E. The narrow fracture approximation by channeled flow. *Journal of Mathematical Analysis and Applications* 365, 1 (2010), 320–331.
- [36] NICK, H., AND MATTHÄI, S. A hybrid finite-element finite-volume method with embedded discontinuities for solute transport in heterogeneous media. *Vadose Zone Journal* 10, 1 (2011), 299–312.
- [37] ODSÆTER, L. H., WHEELER, M. F., KVAMSDAL, T., AND LARSON, M. G. Postprocessing of non-conservative flux for compatibility with transport in heterogeneous media. *Computer Methods in Applied Mechanics and Engineering* 315 (2017), 799–830.
- [38] PALUSZNY, A., MATTHÄI, S., AND HOHMEYER, M. Hybrid finite element–finite volume discretization of complex geologic structures and a new simulation workflow demonstrated on fractured rocks. *Geofluids* 7, 2 (2007), 186–208.
- [39] PANFILI, P., AND COMINELLI, A. Simulation of miscible gas injection in a fractured carbonate reservoir using an embedded discrete fracture model. In *Abu Dhabi International Petroleum Exhibition and Conference* (2014), Society of Petroleum Engineers.
- [40] PANFILI, P., COMINELLI, A., AND SCOTTI, A. Using embedded discrete fracture models (EDFMs) to simulate realistic

- fluid flow problems. In *Second EAGE workshop on naturally fractured reservoirs* (2013).
- [41] SCHWENCK, N., FLEMISCH, B., HELMIG, R., AND WOHLMUTH, B. I. Dimensionally reduced flow models in fractured porous media: crossings and boundaries. *Computational Geosciences* 19, 6 (2015), 1219–1230.
  - [42] SCOTTI, A., FORMAGGIA, L., AND SOTTOCASA, F. Analysis of a mimetic finite difference approximation of flows in fractured porous media. *ESAIM: Mathematical Modelling and Numerical Analysis* (2017).
  - [43] SUN, S., AND WHEELER, M. F. A posteriori error estimation and dynamic adaptivity for symmetric discontinuous Galerkin approximations of reactive transport problems. *Computer Methods in Applied Mechanics and Engineering* 195, 7-8 (2006), 632–652.
  - [44] TENE, M., BOSMA, S. B., AL KOBALSI, M. S., AND HAJIBEYGI, H. Projection-based embedded discrete fracture model (pEDFM). *Advances in Water Resources* 105 (2017), 205–216.